Driving Saturn's magnetospheric periodicities from the upper atmosphere/ionosphere: Magnetotail response to dual sources

Xianzhe Jia[1] and Margaret G. Kivelson[1,2]

Received 31 July 2012; revised 7 October 2012; accepted 14 October 2012; published 28 November 2012.

[1] Despite the high degree of axial symmetry of Saturn's internal magnetic field, rotation-associated periodicities are evident in Saturn's electromagnetic radiation, its magnetic perturbations and its particle populations. Although close to the mean rotation period of the cloud tops, the electromagnetic period drifts slightly over a time scale of years and, at high latitudes, differs for sources in the north and south. The source of the periodicity remains a mystery. The model investigated here places the momentum source in the upper atmosphere/ionosphere, with the wind patterns in the two hemispheres rotating about the spin axis at different rates typical of the 2005–2006 southern summer for which Cassini data have been extensively analyzed. A source at low altitudes would account for the persistence of phase following solar wind disruption of magnetospheric flow patterns but might not produce appropriate magnetospheric responses. However, a magnetohydrodynamic simulation in which vortical winds in the ionosphere drive field-aligned currents into the magnetosphere shows that the dual sources account nearly quantitatively for many measured magnetospheric responses. This paper focuses on the magnetotail where the model is shown to reproduce many well-documented results of data analysis including the features that appear distinctly at each of the two periods and those that appear as a carrier signal with amplitude modulation and phase shifts. In particular, the model accounts for current sheet flapping and modulation of the plasma sheet thickness and for the periodic structure of density enhancements at high latitudes at different periods in the north and the south.

Citation: Jia, X., and M. G. Kivelson (2012), Driving Saturn's magnetospheric periodicities from the upper atmosphere/ionosphere: Magnetotail response to dual sources, *J. Geophys. Res.*, *117*, A11219, doi:10.1029/2012JA018183.

1. Introduction

[2] Images of Saturn and the other giant planets track the motions of their cloudy tropospheres but do not reveal the rotation rates of their deep interiors. From images it is clear that Saturn rotates with a period of 10.5 to 10.8 h; additional geophysical analysis is consistent with the shorter rotation period [*Anderson and Schubert*, 2007]. Numerous electromagnetic, plasma and auroral phenomena vary with roughly the same period [*Andrews et al.*, 2008, 2010a, 2011, 2012; *Arridge et al.*, 2011; *Carbary and Krimigis*, 1982; *Clarke et al.*, 2010a, 2010b; *Cowley et al.*, 2006; *Espinosa and Dougherty*, 2000; *Espinosa et al.*, 2003a, 2003b; *Galopeau and Lecacheux*, 2000; *Gurnett et al.*, 2005, 2007; *Lecacheux et al.*, 1997; *Mitchell et al.*, 2009; *Nichols et al.*, 2010]. Initially the periodic modulation of power in Saturn's kilometric radiation [*Warwick et al.*, 1981] was taken to arise from magnetic asymmetries of the deep interior [*Desch and Kaiser*, 1981; *Seidelmann et al.*, 2002]. However, it was later realized that the period drifts by as much as ~1%/yr, that the period differs slightly for sources in the north and south and that it varies with season [*Lecacheux et al.*, 1997; *Kurth et al.*, 2007; *Gurnett et al.*, 2005, 2009a, 2009b, 2010a; *Lamy*, 2011]. The drift of the period and its duality implies that the source of the signal is not the deep interior of the planet, so attention has recently focused on identifying a plausible generation mechanism for the rotational asymmetry.

[3] Various models have been suggested. All models require that there be structure with $m = 1$ azimuthal symmetry in the frame of the rotating signal, but none explains why such symmetry dominates, other than because the data require it. *Espinosa et al.* [2003b] proposed that a fast mode wave is launched periodically from a restricted range of longitudes, but did not identify the source of the wave. *Southwood and Kivelson* [2007] found that some features of the magnetic periodicity in the inner magnetosphere and the plasma sheet require a rotating pattern of field-aligned currents (FACs) that flow between the northern and southern

[1]Department of Atmospheric, Oceanic and Space Sciences, University of Michigan, Ann Arbor, Michigan, USA.
[2]Department of Earth and Space Sciences, University of California, Los Angeles, California, USA.

Corresponding author: X. Jia, Department of Atmospheric, Oceanic and Space Sciences, University of Michigan, 1411B Space Research Bldg., 2455 Hayward St., Ann Arbor, MI 48109-2143, USA. (xzjia@umich.edu)

0148-0227/12/2012JA018183

hemisphere ionospheres (referred to as the cam current). This model was developed to account for the nature of the rotating magnetic perturbations in the equatorial magnetosphere but did not identify the mechanism that generates the required currents. Analogous arguments, based on studies of the magnetic perturbations, were put forward by *Andrews et al.* [2010a, 2010b, 2011] and *Provan et al.* [2009, 2011], who provided schematic images of the magnetic field fluctuations varying at what we will refer to as the rotation period. *Southwood and Kivelson* [2009] argued that the cam current system can account for the periodic intensification of Saturn kilometric radiation (SKR) as the upward current from the southern hemisphere rotates into the morning sector, thus linking the observed equatorial magnetic perturbations to radiofrequency emissions from the ionosphere.

[4] Other authors have focused on rotating flow anomalies in the equatorial magnetosphere as the source of rotational modulations [*Goldreich and Farmer*, 2007; *Gurnett et al.*, 2007]. *Khurana et al.* [2009] attributed the periodicity to "semipermanent azimuthal anomalies in the ring current region in the fluxes of energetic charged particles, plasma density, magnetic field, and electrical current with a longitudinal wave number $m = 1$." In the models that focus on equatorial convection as the source of the rotational modulation, the structure is thought to develop as a natural interchange instability of magnetospheric plasma, fed by a source at the orbit of Enceladus and rotating at the observed period. The models do not suggest a mechanism for imposing the rotational phase on the proposed rotating convective flow pattern following magnetospheric disruptions that occur at times of extreme solar wind conditions (but see *Southwood* [2011b]). Various observations over many years indicate that persistent discontinuities of phase in the periodic signals do not occur [*Andrews et al.*, 2011], and we have suggested [*Jia et al.*, 2012a] that even if for unspecified reasons an $m = 1$ interchange pattern is favored in the equatorial magnetosphere, the phase persistence presents a problem. The persistence of rotational phase appears to us to argue against an equatorial driver. In section 6, we elaborate on this matter.

[5] If the source of the periodicity is not in the equatorial magnetosphere, it may be in the atmosphere and the ionosphere. The lower atmosphere (i.e., the troposphere) has been systematically imaged and those images do not reveal structures with the required low-order azimuthal symmetry. On the other hand, as yet we know nothing about the azimuthal structure and flows at the higher levels of the atmosphere (i.e., the thermosphere) that interact directly with the ionosphere, and the wind patterns may change with altitude. In a previous paper [*Jia et al.*, 2012a], we argued that a plausible locus for a relatively stable momentum source of axially asymmetric perturbations in the ionosphere is the upper atmosphere, a region with inertia high enough to maintain approximate persistence of both period and phase of an axially asymmetric structure but not so massive as to preclude slow variations (~1%/yr) of its rotation period. For sufficiently high vertical momentum transport rates, rotational asymmetry in the upper atmosphere would couple into the ionosphere through collisions. In order to couple the ionosphere to the magnetosphere, the perturbations must generate FACs. Flow shears generate FACs, so we proposed that the ionosphere is perturbed by localized vortical flows steady in a frame rotating at a specified period. Because the momentum source was nominally located in the upper atmosphere, the rotating perturbations would not respond significantly to magnetospheric disturbances associated with solar wind variability and could repeatedly reestablish a system of FACs without significant phase jumps.

[6] In order to understand how the magnetosphere would respond to the assumed ionospheric source of rotational asymmetry, we carried out a simulation using the global three-dimensional magnetohydrodynamic (MHD) model BATSRUS (Block Adaptive Tree Solar wind Roe-type Upwind Scheme) [*Powell et al.*, 1999; *Gombosi et al.*, 2002, 2004] together with an Ionosphere Electrodynamics (IE) solver [*Ridley et al.*, 2004] that had previously been used to model Saturn's magnetosphere [*Hansen et al.*, 2000, 2005; *Gombosi and Hansen*, 2005; *Zieger et al.*, 2010; *Jia et al.*, 2012a, 2012b]. Further details of the global MHD model are provided in Appendix A. Modifying earlier versions of the BATSRUS code to include the prescribed vortical flow in the southern ionosphere, we were able to test how the magnetosphere would respond to the hypothesized rotating ionospheric asymmetry. Initially both the vortical perturbations and the global ionosphere were set into rotation at the 10.8 h period relevant to the southern SKR source in the postsolstice years of 2005 and 2006, but the ionosphere subsequently slowed through interaction with the magnetosphere, while still being perturbed by flow vortices rotating at the imposed period.

[7] Lacking direct evidence of the form of the flow, we imposed streamlines that varied with latitude and longitude as in a latitudinal cycle of a degree 15 spherical harmonic, selecting the cycle (between the two neighboring nodes at ~65° and ~76° southern latitude) centered at ~70° south latitude so that the FACs would be centered on a magnetic shell on which the observed FACs peak [*Southwood and Kivelson*, 2007]. The wind speeds were set to produce the magnitude of the perturbations of the equatorial magnetic field inside of ~12 R_S reported from data [*Southwood and Kivelson*, 2007; *Andrews et al.*, 2008]. As we desired to investigate internally driven periodicities, we maintained fixed solar wind conditions consistent with a quiet magnetosphere. Without adjusting parameters further, we found that the model reproduces nearly quantitatively many of the dominant observed periodic responses of the magnetospheric system. For example, the periodic excursions of the magnetopause and bow shock were found to be displaced through a range of distances consistent with observations [*Clarke et al.*, 2010a, 2010b], the flapping of the magnetotail current sheet was consistent with the range of positions reported as a function of downtail distance [*Khurana et al.*, 2009], and the intensity of the rotating FAC flowing upward from the southern ionosphere was found to vary with local time in a manner that follows closely the observed local time variation of SKR power [*Lamy et al.*, 2009]. Like other models proposed to this time, our MHD simulation simply postulates a rotating $m = 1$ asymmetry in the upper atmosphere and does not provide a physical model that explains how this particular low-order asymmetry to develop from first principles. However, the success of the model in reproducing many features of observed magnetospheric

perturbations has led us to believe that the model is worth probing further.

[8] In our first runs [*Jia et al.*, 2012a], we introduced vortical flow only in the high-latitude southern ionosphere. Emboldened by the initial success of our model, we report here on additional runs in which we have extended our model by adding vortical structures in the northern ionosphere rotating at the northern SKR period (10.6 h) observed during the years 2005–2006 [*Gurnett et al.*, 2009a, 2009b, 2010a; *Lamy*, 2011; *Southwood*, 2011a]. In section 2 we present details of the new simulation. In section 3 we focus on the properties of the magnetotail that vary through the beat period of ~23 days between the northern and southern periods, showing that at fixed equatorial locations, the variations over many rotation periods of the simulated magnetic perturbations can be described approximately in terms of beats between two sinusoidal signals with different amplitudes at closely spaced frequencies. We find that the form of the signal changes with radial distance in a way that can be understood by recognizing that the relative power imposed from the two sources depends on the L shell examined. In section 4 we examine the flapping of the current sheet, showing that the observed north-south motion of the current sheet location is consistent with the Cassini observations as analyzed by *Khurana et al.* [2009], *Arridge et al.* [2011] and *Provan et al.* [2012]. We show that our model also reproduces the phase-dependent variations of plasma sheet thickness reported by *Provan et al.* [2012]. In section 5, we identify the source of periodic modulation of plasma density observed on high-latitude orbits, finding that the model accounts for observations of variations of plasma density at the northern period in the north and the southern period in the south [*Gurnett et al.*, 2010b]. In section 6 we return to the issue of the persistence of signal phases despite large-scale temporal changes of the magnetosphere in response to changes of external solar wind conditions. In section 7, we summarize the key results and discuss expectations for the next solstice season.

2. Simulation With Both Southern and Northern Sources of Field-Aligned Currents

[9] The question to be addressed in this paper is how the magnetotail responds to vortical ionospheric anomalies rotating about the spin axis at different rates in the north and in the south. We modify the MHD simulation of *Jia et al.* [2012a] that considered the magnetosphere response to a vortical flow pattern localized in the southern ionosphere and rotating with a 10.8 h period by adding a second source in the north that rotates about the spin axis in 10.6 h. As in our earlier work, we use not only different frequencies but also different conductances in the northern and southern ionospheres (1 S and 3 S, respectively, for the Pedersen conductance) to approximate conditions valid in 2005–2006, the years in which many analyzed measurements made by instruments on the Cassini Orbiter are available for comparison.

[10] We had to decide where to place the center of the vortices in the north and how to characterize the flow magnitude. We had been guided in our localization of the southern source by evidence that the most intense rotating FACs peak on flux tubes whose invariant latitude is 70° [*Southwood and Kivelson*, 2007]. For this reason, we modeled the vortical perturbation flow in the south in terms of one cycle of the spherical harmonic $Y_{15,1}(\theta, \phi)$ that lies between the two neighboring nodes at ~65° and ~76° southern latitude and is centered near the latitude of 70° for all longitudes. No analogous direct evidence is available to identify the central latitude of a northern source. However, *Provan et al.* [2011] and *Andrews et al.* [2012] report that near the equator, the intensity of magnetic perturbations modulated at the northern period is roughly 1/3 the intensity of the signal modulated at the southern period in the 2005–2006 period, suggesting that the northern source was weaker than the southern source. On the other hand, *Cecconi et al.* [2009] show that the northern SKR source is at a few degrees higher latitude than the southern source. In an attempt to represent both of these features, we modeled flows in the northern ionosphere as vortices centered at 75° northern latitude for which we selected one cycle (between the two neighboring nodes at ~71° and ~80° northern latitude) of a spherical harmonic of degree 21 and order 1, using the same amplitude factor as that used for the southern hemisphere vortices. The slight difference in the latitudinal spread of the northern and southern vortices is of little consequence as the feature of significance for the simulation is the current intensity. For this assumed amplitude factor, the perturbation electric fields ($E = -v \times B$) differ little in the two hemispheres, so the current densities ($j = \sigma E$) differ principally because of the different conductivities, yielding FACs in the north ~1/3 as strong as those generated in the south. Small departures from the ratio of 1/3 result from the slightly different surface magnetic fields near 70° latitude and near 75° and the slightly different spatial scales and flow speeds obtained from the spherical harmonic representations. Because the magnitude of magnetic perturbations in the equatorial magnetosphere remain relatively constant in magnitude everywhere inside a cam current system (i.e., a system of FACs flowing from ionosphere to ionosphere and varying roughly sinusoidally with rotation phase), the relative magnitudes of equatorial magnetic perturbations interior to the rotating current pattern are relatively insensitive to the latitude on which it is centered. On the other hand, the high-latitude response should vary with the latitude of the source currents and a weak northern source extending into the high-latitude polar cap should, in principle, impose a signal at high northern latitudes comparable in strength to that on high-latitude southern flux tubes arising from a stronger, but more remote, southern source.

[11] The simulation is set up as described in detail by *Jia et al.* [2012a]. As in the previous run, we adopt steady solar wind conditions with nominal parameters: plasma mass density of 0.05 amu/cm^3, flow velocity of 400 km/s orthogonal to Saturn's spin axis, temperature of 20 eV, and a southward interplanetary magnetic field (IMF) of amplitude 0.5 nT. The field orientation inhibits reconnection at the magnetopause. The treatment of the inner boundary, located on a sphere at 3 R_S, the parameters used for the neutral mass sources at the orbits of Enceladus and Titan, and the contribution of ionization and charge exchange are described in that earlier paper. For a simulation with drivers at two slightly different frequencies, we are interested in understanding responses on time scales longer than the beat period

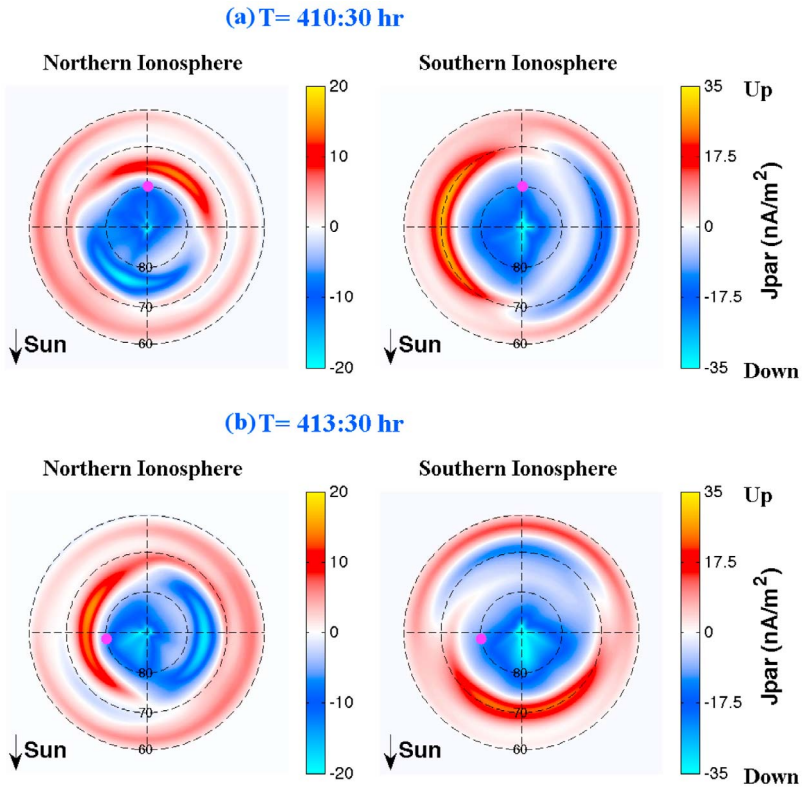

Figure 1. Currents into (blue) and out of (red) the ionosphere in the north and south, viewed from the north. From the simulation with a source of vorticity centered at 75° northern latitude, rotating with a 10.6 h period and a second source at 70° southern latitude rotating at a 10.8 h period. Field-aligned current (color bar) flows into and out of both ionospheres. (Color bars cover different ranges for the two hemispheres.) A small magenta ball is a marker of rotation phase that indicates the direction of the equatorial magnetic perturbation arising from the southern source. The initial relative phase between the two sources is arbitrary. The strongest currents in each hemisphere are found near the centers of the vortices. (a) Taken at hour 410:30 at a rotation phase when the southern FAC produces equatorial radial magnetic perturbations that point antisunward. (b) Taken at hour 413:30 when the northern FAC produces equatorial radial magnetic perturbations that point sunward.

(~23 days) between the northern and southern periods, so the run was extended for 1000 h.

[12] After the run has stabilized, FACs flow into and out of the ionosphere. The current pattern is illustrated in Figure 1 at two time steps selected so that the equatorial magnetic perturbation imposed from the southern source points (1) antisunward or (2) toward dawn. The most intense currents are those driven by the rotating vortical winds that we impose in the ionosphere. The color bars differ for the northern and southern hemispheres and the imposed current source is less extended in the north than in the south. The consequence is that the integrated current outward (inward) is substantially larger from the southern source than from the northern source. Currents from both ionospheres couple to the magnetosphere where they feed corotation enforcement currents [*Hill*, 1979; *Vasyliūnas*, 1983], but some portion of the current flows from one hemisphere to the other. It is the localized currents driven by the imposed vortical flows that produce periodic phenomena throughout the magnetosphere in our simulations.

[13] On a global scale, the response of the system differs little between the runs with only one periodic source and with two sources. The perturbation currents imposed by the ionosphere cause the entire system to expand and contract periodically, they produce plasmoids that expand toward the morning side of the magnetotail, and lead to flapping of the plasma sheet, *etc.* However, the presence of perturbations at a second period becomes clear in many measureable phenomena. For example, the tail current sheet moves periodically relative to the equator, but the amplitude of the oscillation and even the sign of the displacement are modulated at the beat period. Perturbations of the flow velocity are little affected in the inner magnetosphere but at and beyond the orbit of Rhea (~9 R_S) the presence of two frequencies significantly modifies the temporal variation. Of particular interest is the development of bulges above the surface of the plasma sheet that travel down tail, with the bulges on the northern boundary recurring at the northern period while the bulges on the southern boundary recur at the southern period. Consequently, the relative locations of bulges on the northern and southern boundaries of the

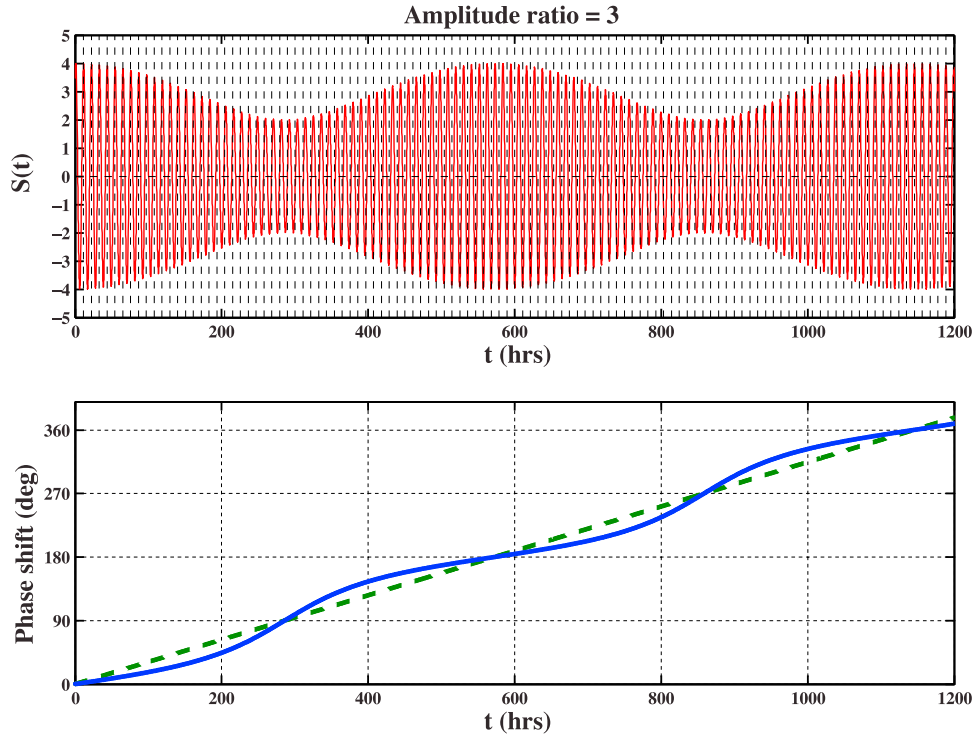

Figure 2. (top) Amplitude and phase drift of a signal formed by superposition of two signals of the form $\cos(\phi - \omega_1 t)$ and 1/3 $\cos(\phi - \omega_2 t)$ over slightly more than two beat cycles of 572.4 h. Vertical lines are separated by the mean period, $2\pi/\omega_m$. (bottom) The quantity $\lambda(t)$ defined in equation (3) is plotted as blue line. The dashed green line shows the variation of $\omega_b t/2$, the additional phase contribution in equation (4). The difference between the dotted green and blue curves (both positive and negative) represents the phase shift relative to a signal varying at frequency ω_1.

plasma sheet vary from one cycle to the next. We will discuss these and other features of the simulation in some detail below.

3. Plasma Sheet Responses and the Beat Period Between Southern and Northern Sources of Field-Aligned Currents

3.1. Properties of a Dual-Frequency Signal

[14] Having adopted the periods 10.8 h in the south and 10.6 h in the north, we start by showing how the closely spaced frequencies of the two sources affect various properties of the tail plasma sheet extracted from the simulation and we compare our results with observations. The sum of two signals of identical amplitude and differing frequencies, ω_1 and ω_2 is known to oscillate at the mean frequency, ω_m, with amplitude varying sinusoidally between 0 and 2 at the beat frequency, ω_b, where

$$\omega_m = \frac{1}{2}(\omega_1 + \omega_2);\ \omega_b = (\omega_1 - \omega_2) \tag{1}$$

If two signals of different amplitude (1 and α) and slightly different frequency, are superposed, the net response $S(t)$ can be written as

$$S(t) = \cos(\omega_1 t - \phi) + \alpha \cos(\omega_2 t - \phi) \tag{2a}$$

$$S(t) = \left\{1 + \tan^2[\lambda(t)]\right\}^{1/2}(1+\alpha)\cos(\omega_b t/2)\cos(\omega_m t + \lambda(t) - \phi) \tag{2b}$$

where we have chosen $t = 0$ as a time when the two signals are in phase, and define

$$\tan\lambda(t) = \frac{(1-\alpha)}{(1+\alpha)}\tan\omega_b t/2;$$

$$\lambda(t) = \tan^{-1}\left[\frac{(1-\alpha)}{(1+\alpha)}\tan\omega_b t/2\right] \pm n\pi \tag{3}$$

Various properties of $S(t)$ differ from those familiar for signals of identical amplitude. The envelope of the amplitude is nonsinusoidal with maximum to minimum values given by $(1 - \alpha)/(1 + \alpha)$. The carrier signal drifts in phase with specifics depending on whether one asks about the drift relative to a signal of frequency ω_m or ω_1. In Figure 2, we plot $S(t)$ and $\lambda(t)$ and $\omega_b t/2$ for $\alpha = 3$, $\omega_1 = \frac{2\pi}{10.6}$h and $\omega_2 = \frac{2\pi}{10.8}$h. In the Figure 2 (top), vertical lines mark the mean period, $(2\pi/\omega_m)$. Slightly more than two beat periods of the signal are shown. Analyzed relative to the mean period, the amplitude, taken to peak at the first marker, shifts right with time until it is strictly out of phase after one beat period (572.4 h); it returns to in phase after the second beat period. If the frequency is taken as that of the dominant signal, ω_1, the argument of the cosine function in equation (2b) becomes

$$\omega_1 t + [\lambda(t) - \omega_b t/2] - \phi \tag{4}$$

the phase shift being the quantity in brackets. Figure 2 (bottom) includes the two curves whose difference is the

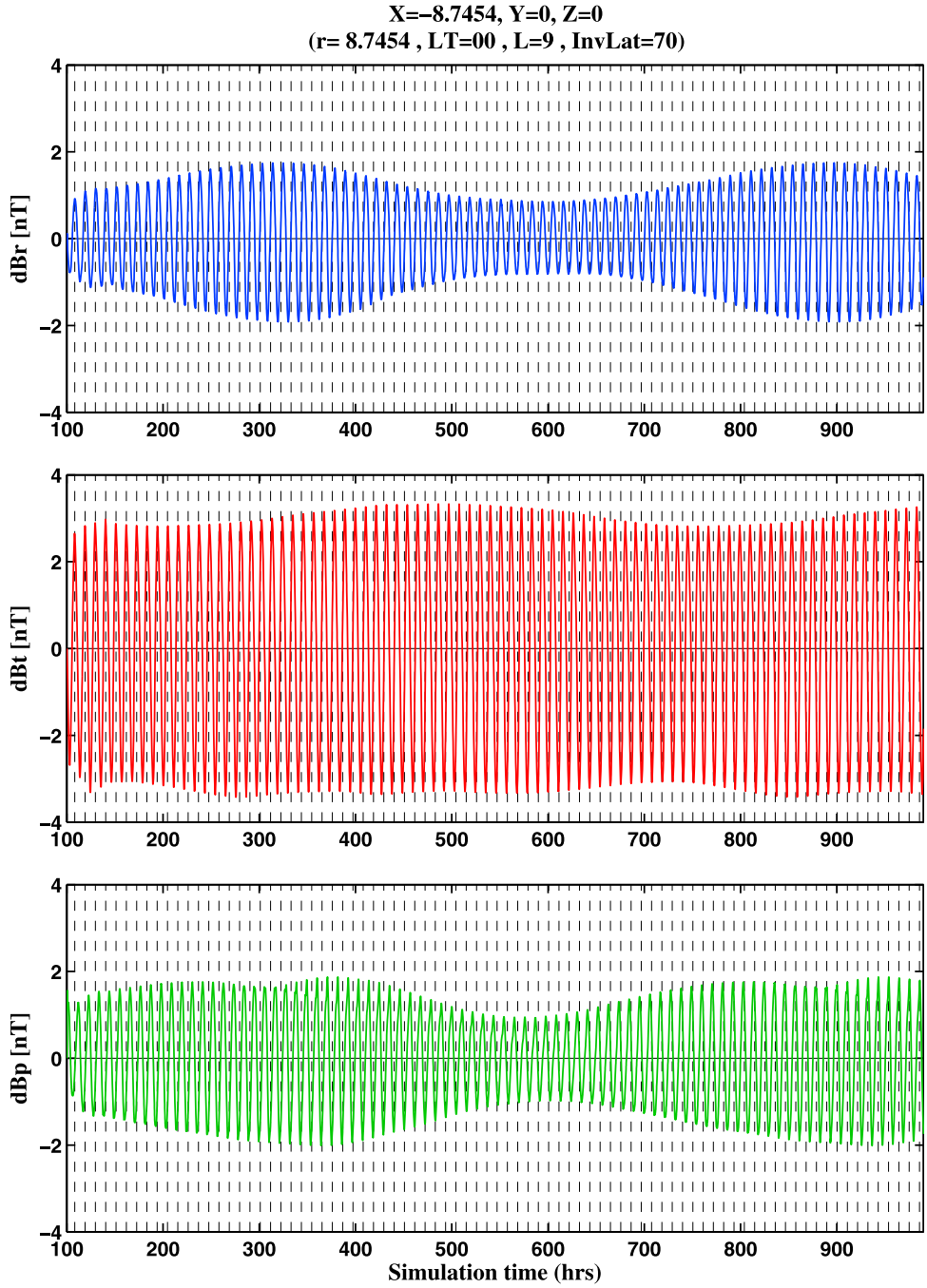

Figure 3. From the simulation with dual frequencies sampled at the equator at 8.74 R_S, three components of the perturbation magnetic field (radial, southward, azimuthal or eastward) followed through approximately two beat cycles of 23.85 days = 572.4 h. Vertical lines are separated by the mean period of 10.7 h to reveal the phase shifts of the simulated signal. The radial and azimuthal components follow closely the variation plotted in Figure 1 for signals of relative amplitude 1/3.

phase shift. This difference takes on both positive and negative values, thus oscillating from leading by about 20° to lagging by the same amount, completing one full excursion in one beat period. It is this oscillation about the dominant period that *Provan et al.* [2011] refer to as "jitter."

3.2. Magnetic Field Perturbations

[15] In Figure 3, we show the three components of the perturbation magnetic field sampled at the equator at 8.74 R_S at local midnight in the simulation. The perturbations were obtained by removing a fit to the field smoothed with a 10.8 h window. The plot covers slightly less than two beat

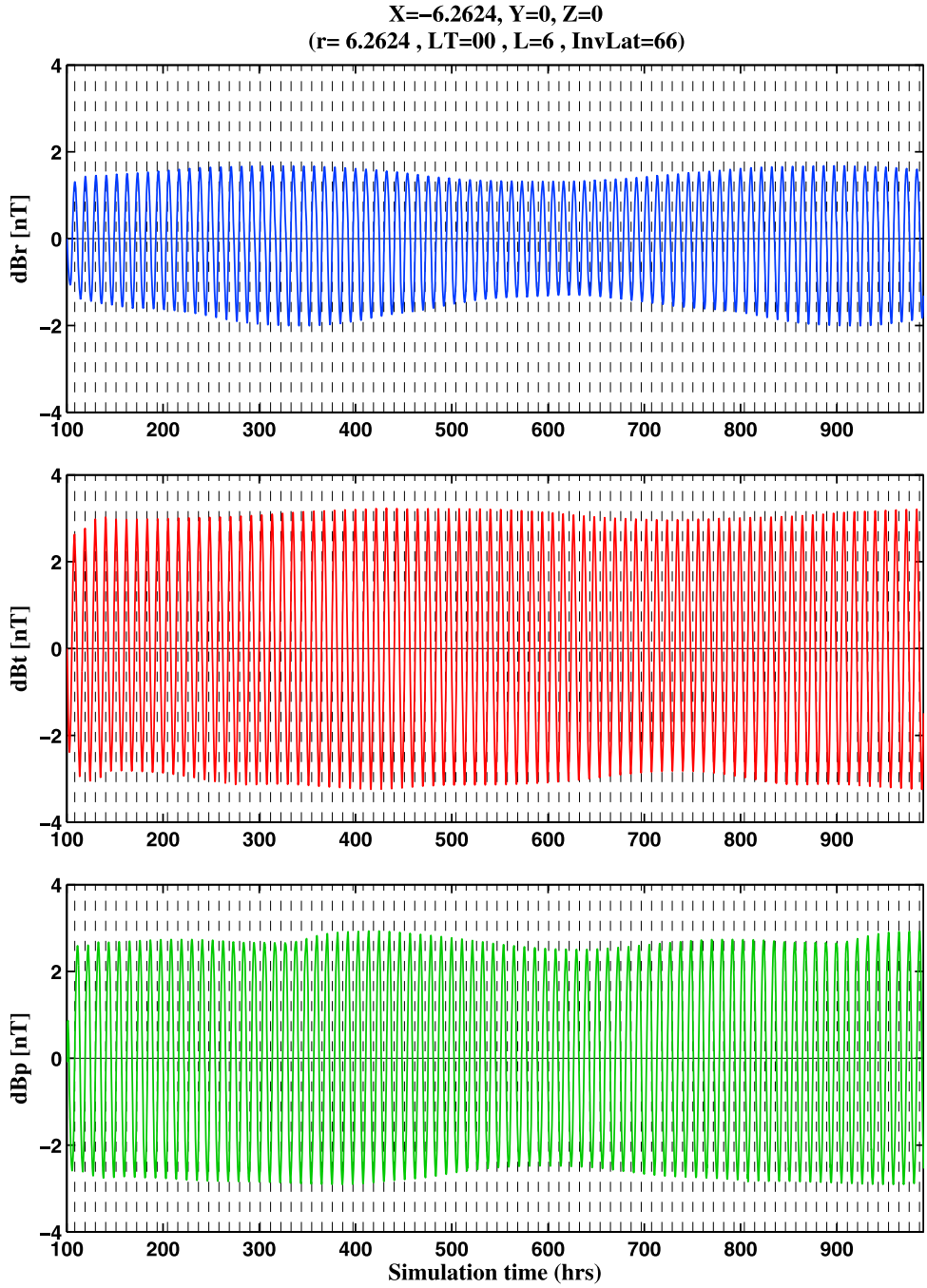

Figure 4. Same as Figure 3 from the simulation with dual frequencies but in this case sampled at the equator at 6.26 R_S. The minimal changes in the envelope of the radial and azimuthal components over a beat period are consistent with a significant difference in amplitude of the two signals.

periods. As the radial and azimuthal components of the background field vanish at the equator, these components respond purely to the FACs coupling the northern and southern ionospheres and thus are good indicators of the relative importance at this location of the two sources. The ratio of the maximum to minimum amplitudes in Figures 3 (top) and 3 (bottom) is close to 2, implying that the power input from the southern and northern signals differs by a factor of ~3 in this portion of the equatorial magnetosphere. Vertical lines, separated by the mean period of 10.7 h help identify phase shifts, which are seen to increase systematically so that at the end of one beat period, the phase has shifted by half a cycle with respect to the reference signal oscillating at the mean period. The envelope of the field-aligned perturbation, dB_θ, varies slightly over the beat period but clearly responds to more complex input than do the transverse components, probably linked to changes in field magnitude arising from periodic "breathing" of the

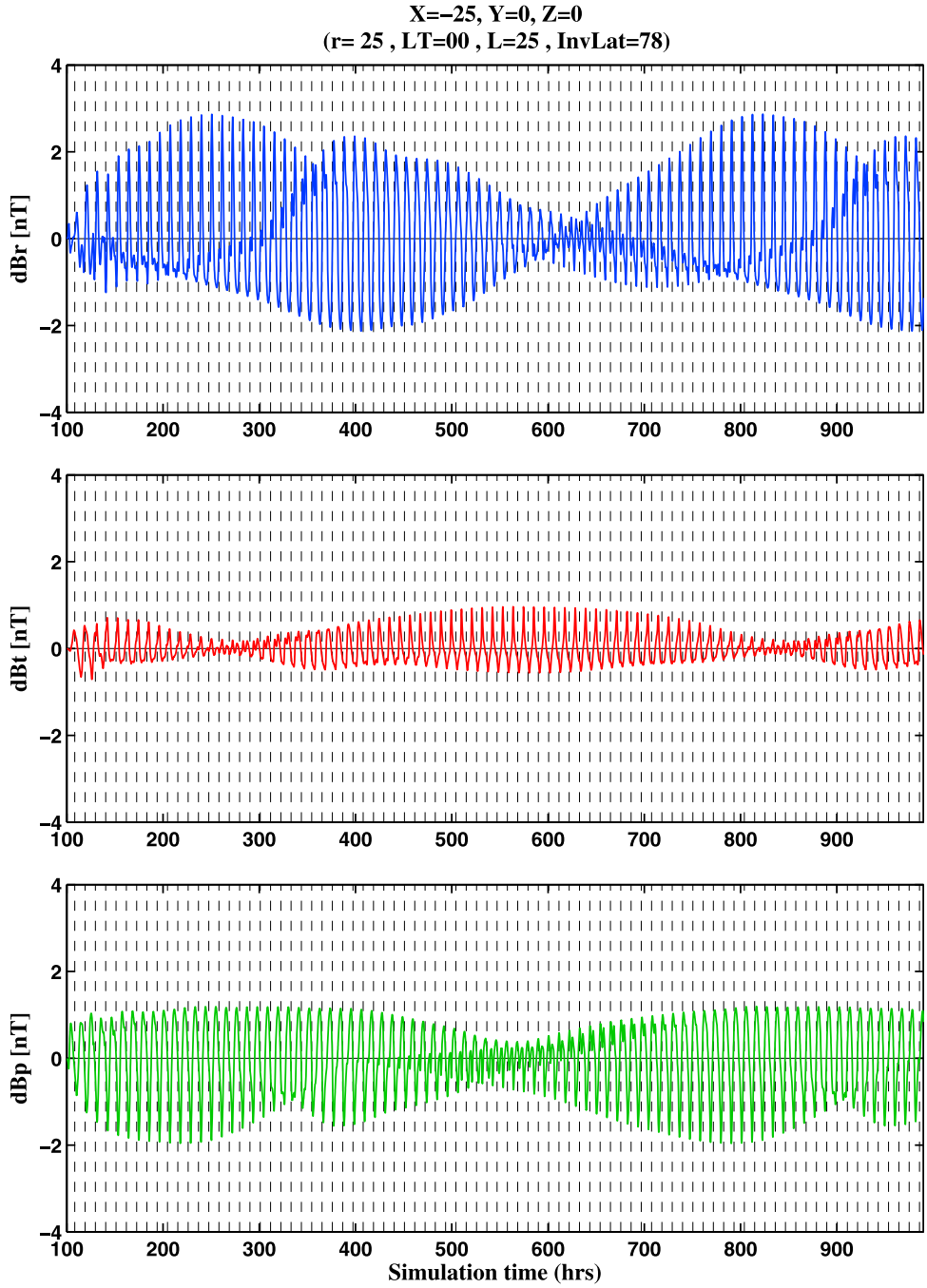

Figure 5. Same as Figure 3 from the simulation with dual frequencies but in this case sampled at the equator at 25 R_S. The signal is less well related to the simple modulation of the radial and azimuthal components shown in Figure 3 because the plasma sheet displacement is nonsinusoidal, as described in section 4, but the strong amplitude modulation of all components at the beat period is consistent with an amplitude ratio of close to 1.

magnetosphere at the rotation period of the dominant southern source [see *Jia et al.*, 2012a, Figure 8] and contributions from a rotating ring current.

[16] Inward of 8.74 R_S one might expect the fraction of the power driven by the higher latitude northern source to diminish slightly. In Figure 4, we plot the magnetic perturbations at 6.26 R_S, again at the equator at midnight. The amplitude of the envelope of the B_ϕ component, for which the periodic signal is always the clearest, varies only by a factor of 1.5, consistent with the expectations from equation (2b) for a ratio of amplitudes of ~1/5. As for Figure 3, the phase of the signal drifts by half a cycle over one beat period.

[17] In the tail plasma sheet the situation is more complex as seen in Figure 5, for which the perturbations were evaluated at the equator at 25 R_S, again on the midnight

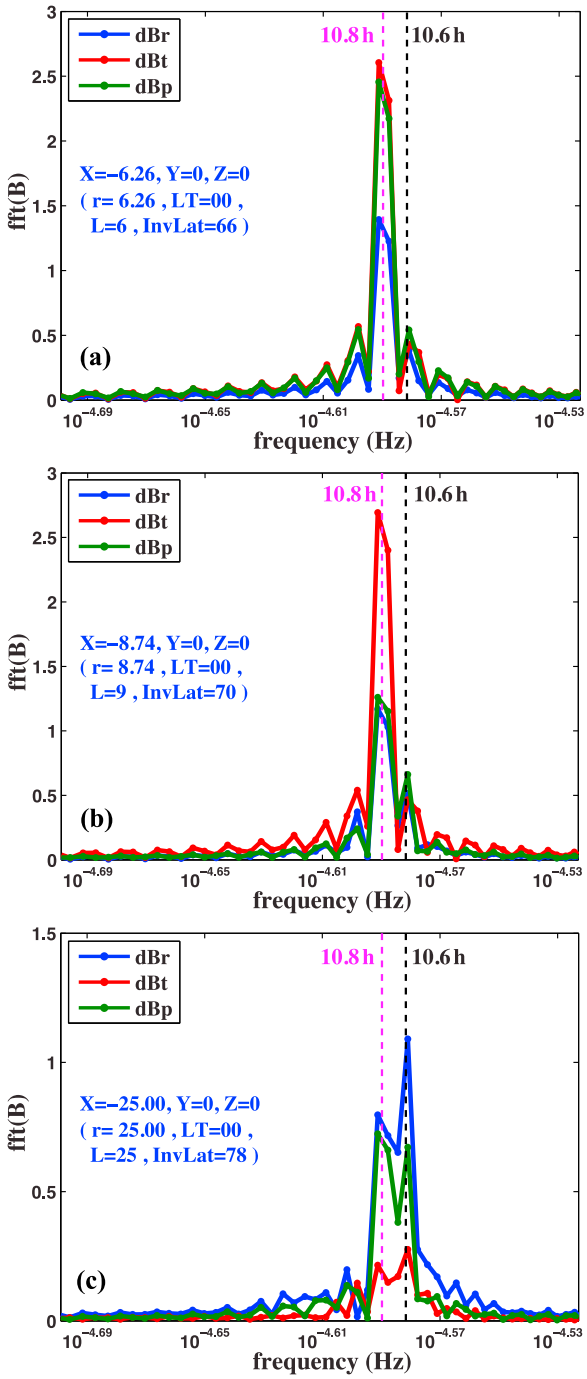

Figure 6. Fourier spectra (amplitude versus frequency) of the magnetic perturbation signals corresponding to (a) Figure 3, (b) Figure 2, and (c) Figure 4 at distances of 6.26 R_S, 8.74 R_S, and 25 R_S.

meridian. Here the signals are far from sinusoidal, so the simple superposition concept is not fully relevant. The direct effect of the FACs linking the two hemispheres is greatly modified by the effect of plasma sheet flapping (i.e., north-south displacement). Nonetheless, systematic phase shifts are again observed, with a shift of half a cycle in one beat period. The beat envelope is clearest for the radial (dB_r) and azimuthal (dB_ϕ), and the large change of magnitude of the envelopes, with peak amplitudes near the time when northern and southern signals are approximately in phase (see Figure 1), is consistent with signals of comparable power.

[18] Fourier transforms of the signals, shown in Figure 6, qualitatively support the inferences from examination of the amplitude envelopes. At 6.26 R_S the amplitude of the signal in dB_ϕ at the southern period is far larger than that at the northern period (5 to 1), at 8.74 R_S the ratio of the amplitudes at the two frequencies is 1 to 2, and at 25 R_S the ratio is close to 1 to 1. The ratio of the amplitudes of the signals at the two frequencies in the radial perturbations has a similar dependence on radial distance. The dB_θ signal is strongly dominated by the signal at the southern frequency in the middle magnetosphere (6.26 and 8.74 R_S) and, although small in amplitude, shows roughly equal input at the two fundamental frequencies in the outer magnetosphere.

[19] Fluctuating magnetic field perturbations are accompanied by other oscillatory phenomena. Of special interest are the components of the flow velocity, which are illustrated in Figure 7. The velocity is shown at 6.26 R_S and 8.74 R_S on the equator at midnight. At both distances, the plasma subcorotates throughout a full cycle. At 6.26 R_S the signals are relatively sinusoidal in form and change little over the 150 h plotted (roughly 1/4 of a beat period), consistent with dominant driving by a single source at the southern frequency. At 8.74 R_S, the form and amplitude of the signals change perceptibly over the 150 h interval and the signal form is not sinusoidal, the effect of dual frequency driving. Measured flow velocities [*Thomsen et al.*, 2010] have substantial uncertainties, but the subcorotation that we extract from the simulation is in the range reported from data. Furthermore, there is evidence of the modulation of the azimuthal velocity at the southern SKR period near the equator between 9 and 12 R_S (K. Ramer, personal communication, 2012).

4. Current Sheet Flapping and Variation of Plasma Sheet Thickness

[20] The current sheet in the tail is known to move up and down periodically, a motion sometimes referred to as flapping [*Carbary et al.*, 2008; *Khurana et al.*, 2009; *Morooka et al.*, 2009; *Arridge et al.*, 2011; *Provan et al.*, 2012]. A notable feature of the flapping that is emphasized by *Khurana et al.* [2009] is that the displacement is not symmetric north and south of the equator. In fact the displacement is typically upward from the equator and back down. The form of the displacement has been attributed to the fact that during the early years of the Cassini mission (until late 2009) the solar wind flow direction was from the south, which warped the plasma disk upward from the equator [*Arridge et al.*, 2008], the description corresponding to an up-down displacement relative to a nonplanar surface lying north of the equator. Because we set the solar wind flow orthogonal to the spin axis in the simulation, our model does not produce a northward warped plasma disk as a result of solar wind-dominated asymmetry. Nonetheless, it does reproduce plasma sheet flapping up from the equator and back. Figure 8 shows a sequence of hourly images in the noon-midnight meridian plane through most of a rotation period that reveal the changing configuration of the magnetotail. In particular one should note that the current sheet (defined by the reversal of the sense of the radial field)

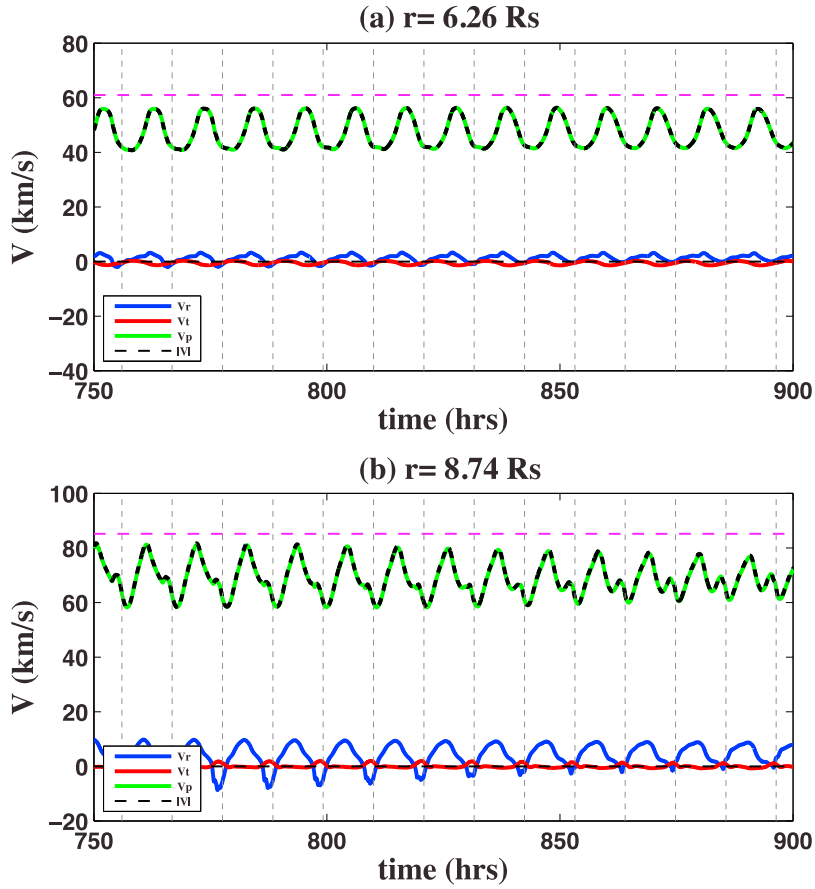

Figure 7. Flow velocity extracted at different radial distances plotted versus time over ~1/4 of a beat cycle. The velocity (blue for radial, red for south-north, green for azimuthal) is measured in the simulation at (a) 6.26 R_S and (b) 8.74 R_S on the equator at midnight. Dashed magenta lines indicate the azimuthal velocity of rigid corotation. Vertical lines are separated by the southern period of 10.8 h.

moves northward and back to the equator. It never moves significantly below the equator. The plasma sheet is seen to thicken and thin through the cycle and there is evidence of perturbations propagating tailward. *Jia et al.* [2012a], using only a source in the south, found that displacements of the current sheet in the midnight meridian plane corresponded well to the data reported by *Khurana et al.* [2009]. They concluded that the southern source must provide net northward momentum to the plasma and that the distortion of the plasma sheet related to the solar wind attack angle is not the primary reason for the observed northward displacement of the average location of the tail plasma sheet inside of a few tens of R_S. Here we conclude that even with dual sources, the stronger source in the south dominates the momentum input to the displacement of the current sheet. Although the flapping motions are dominantly driven by the stronger southern source, aspects of the variations, such as the height of the current sheet above the equator and the thickness of the plasma sheet are strongly affected by the dual sources in ways that we next investigate.

4.1. Effect of Dual Sources on Current Sheet Flapping

[21] Figure 9 shows features of the magnetotail in the dual source simulation on the midnight meridian at 40 R_S downtail over 33 days. Figure 9a shows the height, z_{cs}, of the simulated current sheet above the equator confirming that the current sheet moves predominantly up and back, rarely moving below the equator. The height of the centroid and the amplitude of the periodic excursions of the sheet are modulated at the beat period. Figure 9c shows a plot of the relative phase of the northern and southern signals. When the northern and southern perturbations are in phase, the peak-to-peak amplitude of current sheet flapping is ~4.5 R_S. Half a beat cycle later, the amplitude is ~3 R_S. Figure 10 shows the variation of the current sheet location at several other radial distances, and it can been that the amplitude of current sheet excursions increases with radial distance (from ~1.4 R_S at $x = -20$ R_S to ~6 R_S at $x = -50$ R_S). These features of plasma sheet behavior in the tail are in relatively good agreement with the results of *Provan et al.* [2012], who used Cassini data on inclined orbits to identify the north-south positions of the current sheet over an extended region in the tail and showed that when the two field oscillations are in phase, the current sheet oscillates north-south with a peak-to-peak amplitude of ~3 R_S.

[22] Further information on current sheet properties is provided by *Arridge et al.* [2011], who fit an analytical model to the plasma densities and magnetic signature measured in the vicinity of the flapping current sheet. With ρ_o (taken as 12 R_S) as the distance at which the current sheet

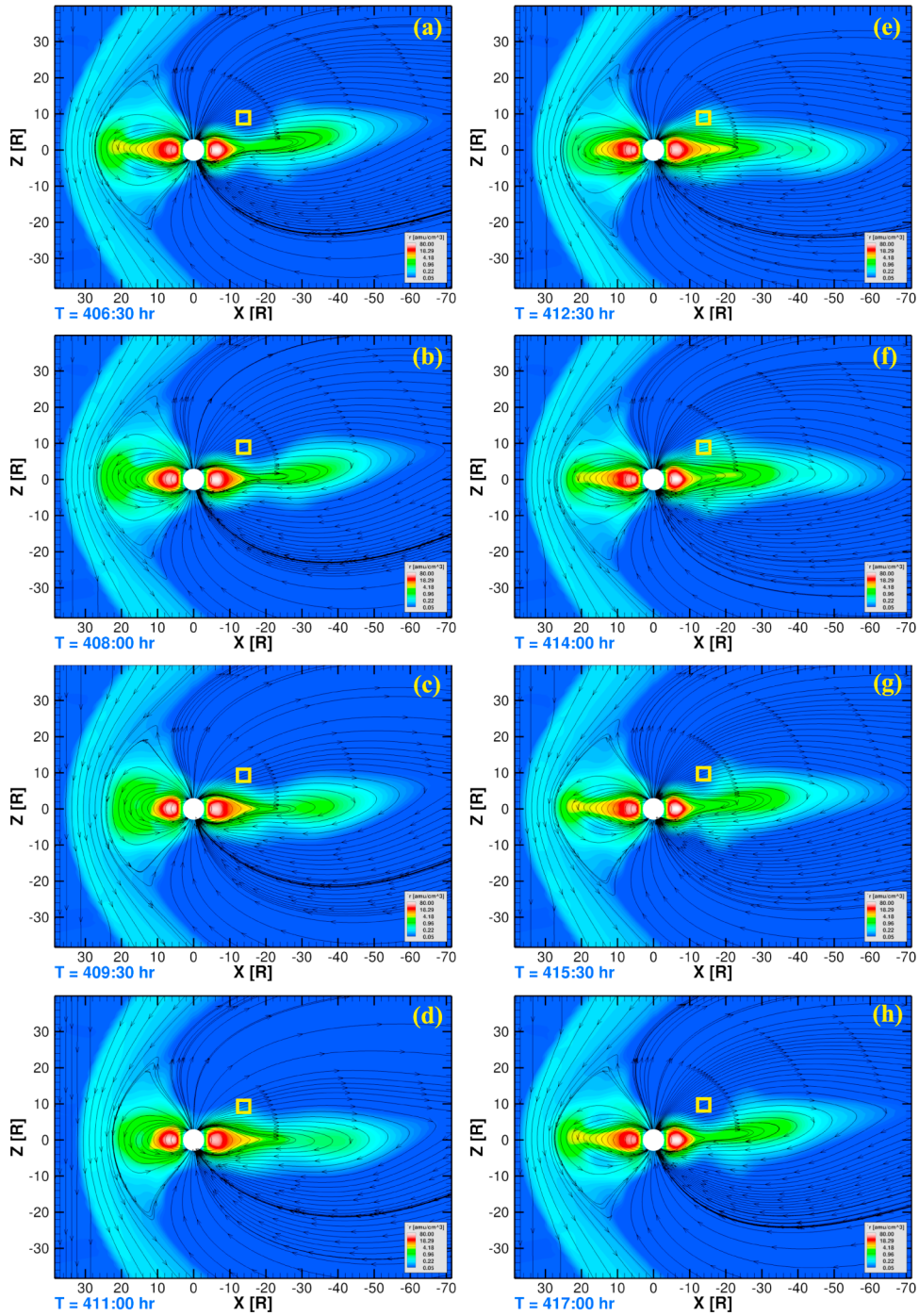

Figure 8. On the midnight meridian the plasma density (color) and field lines every 1.5 h at times labeled in the bottom left corners through one rotation period. The field lines are traced starting from fixed locations arbitrarily distributed in this plane. The yellow box in each image marks a nominal spacecraft location.

begins to tilt and θ_{TILT} (taken as 12°) as the asymptotic tilt angle, identical with the attack angle of the solar wind, they adopt the form

$$z_{CS}(t,\varphi,\rho) = \left[\rho - r_H \tanh\left(\frac{\rho}{r_H}\right)\right]\tan\theta_{SUN} + (\theta_{TILT} - \rho_o)\tan\theta_{TILT}\cos\Psi_{PS}(t,\varphi,\rho)\rho > \rho_o \quad (5)$$

Here ρ is the cylindrical radial distance from the spin axis, Ψ_{PS} is the SLS3 phase [*Kurth et al.*, 2008] of the model plasma sheet oscillations, a function of ρ, time t, the local time of the spacecraft φ; r_H is the hinging distance beyond which the tilt of the current sheet is determined principally by θ_{SUN}, the attack angle of the sun. Fitting the parameters to data from individual nightside orbits, Arridge et al. infer the

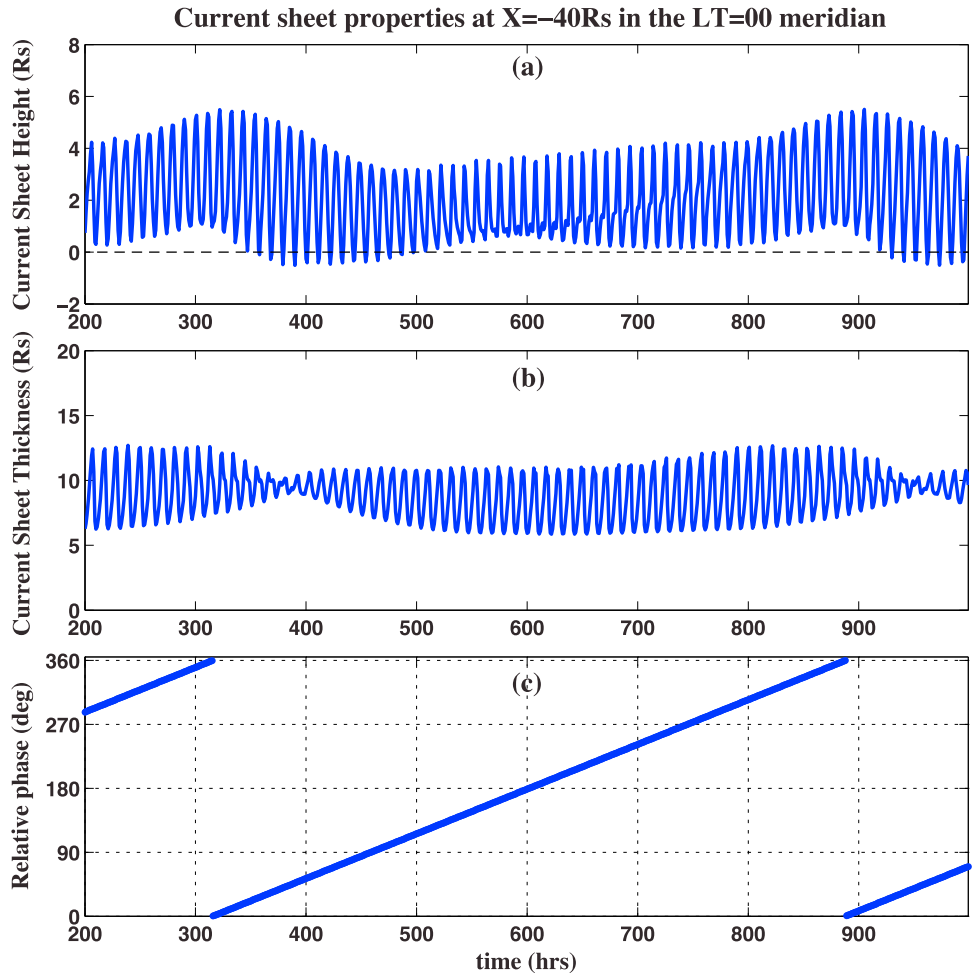

Figure 9. (a) The north-south location of the center of the current sheet, (b) the current sheet thickness, both measured on the midnight meridian at 40 R_S downtail, and (c) the relative phase (north-south) of the imposed B_r perturbation in the equatorial inner magnetosphere plotted versus time over more than one beat cycle.

amplitude and north-south excursion of the current sheet center at a range of distances down the tail.

[23] Because our simulation adopts a solar wind attack angle of 0° and consequently does not produce an asymptotic tilt; values of z_{cs} based on the simulation cannot be directly compared with the values based on Cassini observations, especially at very large distances. Furthermore, as evident from Figure 9, the range of values is sensitive to the beat phase. However, the ρ dependence of the phase delay, $\Psi_{PS}(t, \varphi, \rho)$, in the second term of equation (5) can be directly compared with results from the simulation. Figure 10 shows z_{cs} versus SLS3 southern phase on the midnight meridian of the simulation at four downtail distances. The amplitude of the oscillations varies through a beat cycle, which spreads out the points. Nonetheless, the phase delay versus distance can be obtained by relating the phases of the minima and/or the maxima of the upper envelopes at radial distances between 20 and 50 R_S. The delay is found to be ~4.3°/R_S, a value consistent with those derived from Cassini observations, e.g., 3.4°/R_S from the study of *Carbary et al.* [2007], 3.7° ± 1.4°/R_S as inferred by averaging the parameters given for 11 orbits in Table 2 of *Arridge et al.* [2011] and 2.5°/R_S from the analysis of *Provan et al.* [2012].

4.2. Plasma Sheet Thickness

[24] The plasma sheet does not move rigidly but expands and contracts in thickness every cycle as can be seen in Figure 8. *Provan et al.* [2012] report that the plasma sheet thickness varies over a beat period. They note that when the two driving signals are in antiphase, "the thickness of the current sheet is also strongly modulated during the oscillation by factors of ~2." We have analyzed the thickness of the current sheet at 40 R_S downtail near midnight by fitting the plasma density to a Harris neutral sheet structure, defining the thickness as twice the fitted scale height. Figure 9b shows that the modeled current sheet thickness has a mean of ~8 R_S varying in thickness only slightly when the two signals are nearly in phase but varying roughly by the factor of 2 called for by the observations of Provan et al. over most of the beat period.

5. North-South Asymmetry of Field and Density Perturbations off the Equator

[25] Although both the simulated and the observed magnetic perturbations at relatively low latitudes can be understood in terms of the superposition of signals at the northern and southern periods, magnetic perturbations on open field

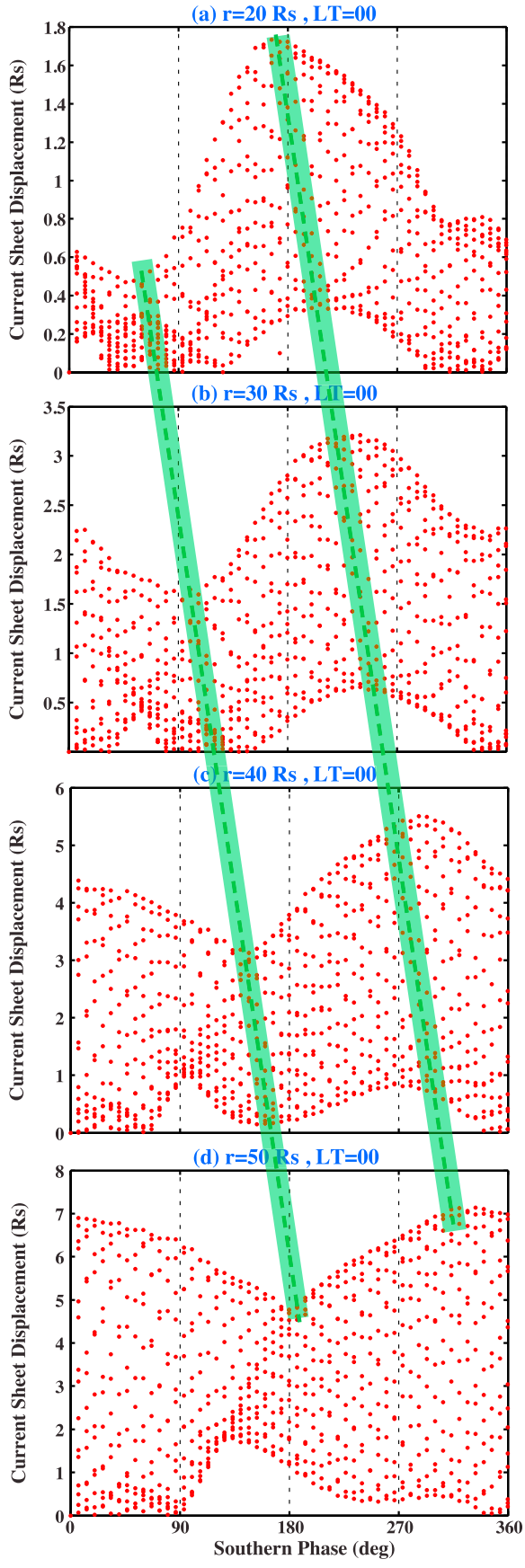

lines at high latitudes appear to be modulated at the frequency characteristic of the hemisphere to which they link [*Andrews et al.*, 2010b, 2012; *Southwood*, 2011a]. In addition, at the interface between closed and open flux tubes, *Gurnett et al.* [2011] and *Provan et al.* [2012] report that features of the plasma and field on what appear to be closed flux tubes vary at the northern SKR period in the north and at the southern period in the south. In this section we show that the dual frequency simulation provides an explanation of these unexpected observations.

[26] Let us first confirm that the signals on the highest dipole invariant-latitude field lines (>80°) differ between north and south in our simulation as they do in observations. On field lines at these high latitudes, *Southwood* [2011a] used a phase-matching technique to demonstrate that magnetic perturbations are driven at different frequencies in the north and south. He selected data from successive oblique orbits whose duration was close to half a beat period. On these orbits Cassini remained on polar cap field lines (invariant latitude >80°) for about 4 days in the south and for about 3 days in the north. In Figure 11a we reproduce Southwood's Figure 3, which shows magnetic field components measured on two of these almost identical, oblique orbits. Southwood found that if he shifted the measurements from the second orbit backward in time by 287 h = 11.96 days, or half a beat cycle, the fluctuations measured at high invariant latitude in the northern hemisphere (following day 52, hour 12) on the two orbits were in phase but the fluctuations in the same invariant latitude range (before day 48 hour 6) in the southern hemisphere were out of phase. This is just what would be expected if the southern hemisphere signal pulsed with a 10.8 h period and the northern hemisphere pulsed with a 10.6 h period.

[27] We have extracted data from the simulation along the orbits used by *Southwood* [2011a]; Figure 11b shows the field components along the orbit plotted as a function of time in the format of Figure 11a. Also plotted are the values from the next orbit in the simulation, time shifted by 287 h. As in the actual measurements, at high invariant latitudes the fluctuations on the successive passes are in phase in the northern hemisphere and out of phase in the southern hemisphere. In the simulation with the IMF strictly southward, even the highest latitude field lines are closed, so one may wonder why the signals are dominated by the nearby sources. We find that in the simulated magnetosphere as in Saturn's actual magnetosphere, most high invariant latitude magnetotail field lines stretch so far down tail that perturbations from one hemisphere decay in amplitude as they propagate down tail and do not reach the opposite hemisphere.

[28] At lower dipole invariant latitudes in the range ~75° to 80°, at the interface between closed and open field lines near the boundary of the plasma sheet, the plasma density

Figure 10. From the MHD simulation, z_{cs} versus the southern phase at (a) −20, (b) −30, (c) −40, and (d) −50 R_S in the midnight meridian over the time plotted in Figure 8. Green lines are approximately aligned with the minimum and the maximum of the oscillation amplitudes at different radial distances. The corresponding phase delay is ~4.3°/R_S, in good agreement with a phase delay of 3.7° ± 1.4°, the average of entries in Table 2 of *Arridge et al.* [2011].

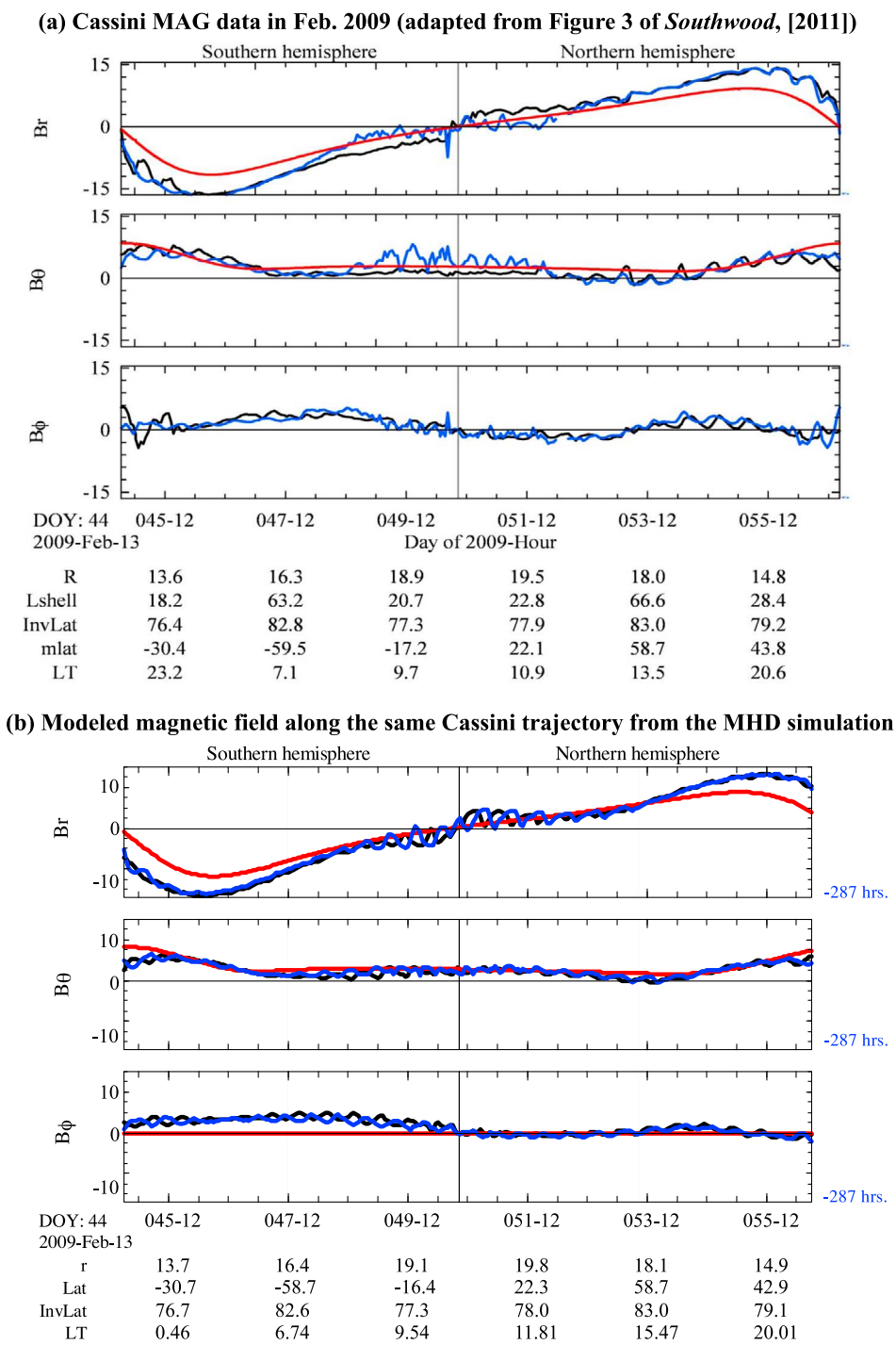

Figure 11. Magnetic field along highly inclined orbits. (a) Cassini data in February 2009 [from *Southwood*, 2011a, Figure 3] and (b) from the dual source simulation along the same orbits. In Figures 11a and 11b the time and orbital information applies to the black traces. The blue traces show data from the next orbit shifted back in time by 287 h = 11.96 days, or half a beat cycle, the shift used by Southwood to match the phases of fluctuations in the northern hemisphere on the successive passes. The red curves show the dipole field contributions.

and the magnetic field components are also modulated at approximately the SKR period of the hemisphere of observation. The density increases and decreases, sometimes with a nearly square wave structure [*Gurnett et al.*, 2010b, 2011]. *Gurnett et al.* [2010b] refer to the rapid density changes observed at high latitudes as "a plasmapause-like density boundary" because the boundary is often quite steep, especially when the orbit is roughly skimming a magnetic L

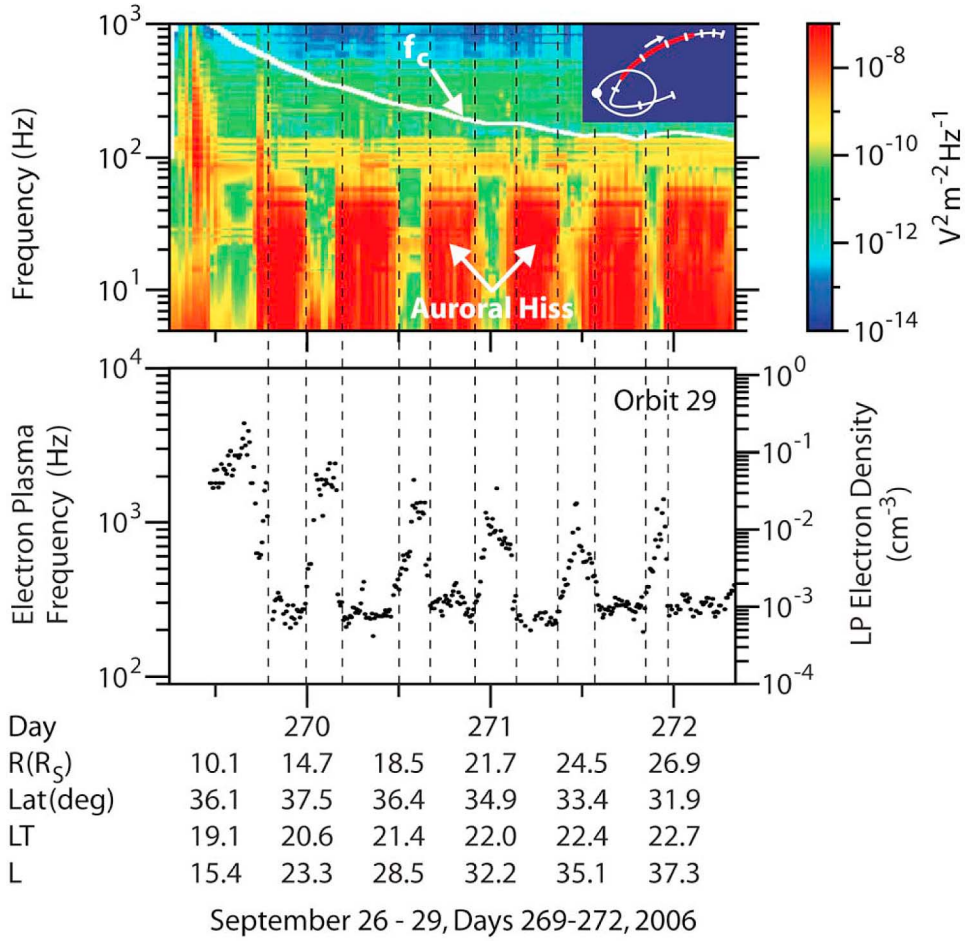

Figure 12. Data for Cassini orbit 29, outbound in September 2006 [from *Gurnett et al.*, 2011, Figure 1]. (top) A dynamic electric field spectrum (frequency versus time with color showing power spectral density) from the Cassini RPWS instrument [*Gurnett et al.*, 2004]. The periodicities were observed along the red portion of the orbit plotted in the insert in the top right inset. (bottom) The electron density (right-hand axis) from the RPWS Langmuir probe.

shell. However, they caution that there is no evidence of a steep density boundary at low latitudes such as that found at the terrestrial plasmapause. An example of the periodic crossings of a density boundary once per rotation period at latitudes >30° and dipole L values >20 is reproduced from *Gurnett et al.* [2011] in Figure 12. Gurnett et al. find periodic signals in the same range of latitude and L shell both north and south. Their analysis shows that the observed periodicities are consistent with SKR periodicities characteristic of the hemisphere of the observations. The high-density region in each hemisphere is centered near midnight at the time of maximum SKR intensity in the relevant hemisphere. In interpreting the results, *Gurnett et al.* [2010b, 2011] put forward models in which a density asymmetry fixed in the rotating frame produces temporal variations in an inertial frame, approximately the spacecraft frame. The MHD simulation suggests a different interpretation.

[29] In the MHD simulation, periodic density increases are indeed present in the vicinity of the orbits investigated by *Gurnett et al.* [2011]. In the simulation, the increases are dynamical responses of the magnetotail plasma sheet to disturbances launched when a particular phase of the ionospheric current system rotates into the midnight sector. The traveling plasma bulges can be identified in "snapshots" of the density distribution in the plasma sheet on the noon-midnight meridian and are shown at different phases of one rotation period in Figure 8. The small yellow boxes in Figure 8 show the approximate location of Cassini on day 270 at the time of the first sharp density increase shown in Figure 12. From 406:30 to 409:30, the density at the location of the box is very low. The density increases significantly at this nominal spacecraft location in the next panel and then remains enhanced for several hours before falling back to the low level of lobe-like flux tubes in Figure 8h. In a movie from which the images are extracted, one can see the bulging density enhancement developing close to Saturn and propagating down the tail. This suggests that the density variations observed in the magnetotail well off the equator are not fixed rotating structures but are dynamical structures sweeping over the spacecraft on their way down the tail. It can be seen that the field magnitude minima correspond roughly to the density maxima.

[30] The measured and modeled density and magnetic field perturbations (a dipole field is subtracted) are quantitatively similar as seen in Figure 13. The primary difference

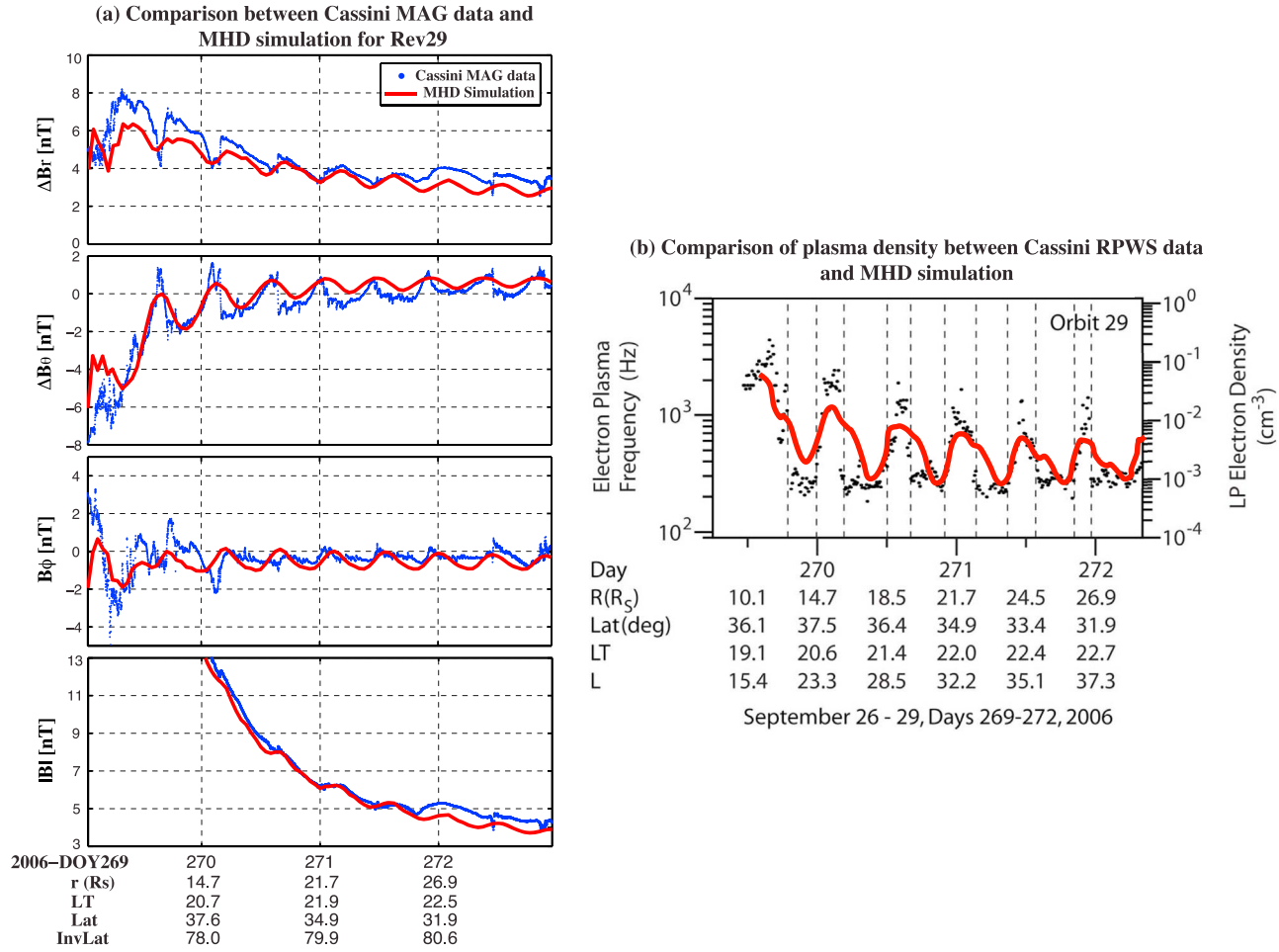

Figure 13. For Cassini orbit 29, (a) the magnetic field components and magnitude (B_r, B_θ, B_ϕ, |B| from top down): blue trace, from measurements of the Cassini Magnetometer [*Dougherty et al.*, 2004]; red trace, extracted from the simulation. (b) Ion density extracted from the simulation (red trace) along orbit 29, superimposed on the measured electron plasma density trace [*Gurnett et al.*, 2011] from Figure 12.

is the steepness of the variation, a smoothing that may in part result from low time resolution (1 h) of the simulated density curve. Although the simulation was run with a time step of 30 s, only hourly data were stored globally because of the daunting size of the output from a run for 1000 h. (At a limited number of positions in the simulation, full time resolution data were stored; for example, the spectra shown in Figure 6 make use of those higher time resolution data.)

[31] The density bulges moving along the boundary of the plasma sheet in successive frames of Figure 8 propagate antisunward in both north and south. From Figure 8, one can estimate the speed at which the bulges of enhanced plasma density propagate down tail. For example, the southern bulge centered at -15 R_S at 414:00 in Figure 8f is centered at -22 R_S at 417:00 in Figure 8h, and thus has traveled at a mean speed of 2.3 R_S/h or about 39 km/s. Comparison of Figures 8f and 8h suggests that the speed in the north is somewhat faster, roughly 3.3 R_S/h or about 55 km/s. The speeds are close to the sound speed in the vicinity of the bulges, which we estimate as 50–60 km/s in the simulation. With the field magnitude and the density in antiphase, the results are consistent with slow mode perturbations propagating along the flux tubes on the boundary of the plasma sheet.

[32] The temporal sequence of Figure 8 can be used to identify the times at which the northern and southern bulges appear. In Figures 8a and 8b, there is no evidence of bulges. In Figure 8c at 409:30, a bulge is just beginning to appear in the south, just beyond -10 R_S. By examining higher time resolution data, we find that 408:30 is a closer estimate. At this time, the peak of the upward FAC in the southern hemisphere is located at approximately 02:00 LT. By the time the center of the bulge has propagated to approximately -15 R_S (410:30), the peak upward FAC in the south is on the dawn meridian, consistent with its expected orientation at the peak of southern SKR intensity [*Provan et al.*, 2012; *Jia et al.*, 2012a]. A new bulge in the north becomes evident only at 411:00 in Figure 8d, or at higher time resolution at about 410:30. At this time the peak upward current from the northern ionosphere is centered at 22:00 LT. Two hours later (about 413:30), the center of the northern bulge has reached -15 R_S and the peak upward FAC from the northern ionosphere is centered at dawn, corresponding to the expected position at the time of peak intensity of northern hemisphere SKR [see *Provan et al.*, 2012]. The speeds implied by timing these displacements inside of -15 R_S differ by less than a factor of 2 from the estimates based on propagation at later

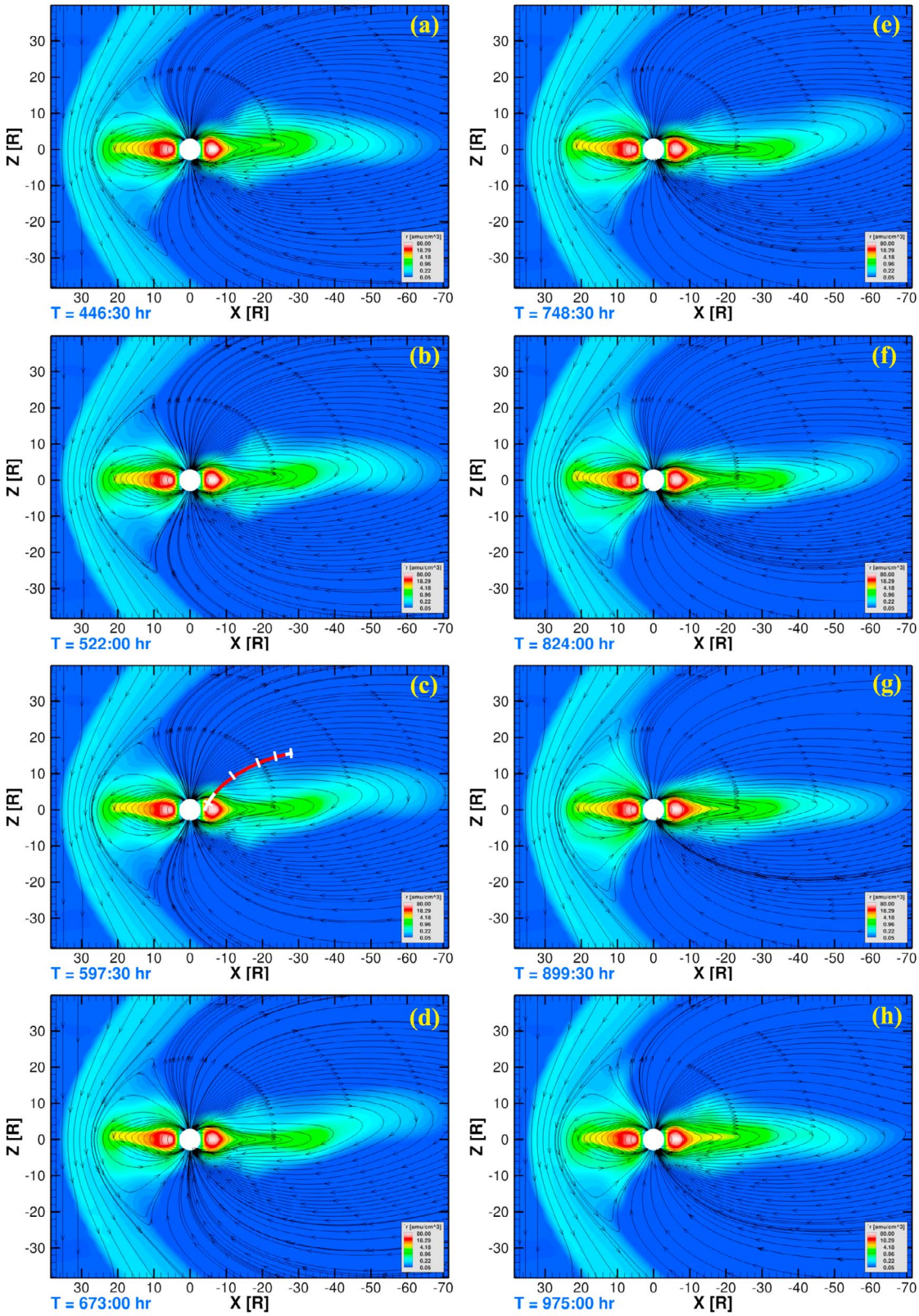

Figure 14. Same as Figure 8 but at simulation times separated by 75.5 h or ~7 southern rotation periods. A portion of orbit 29 [*Gurnett et al.*, 2011] as in Figure 11a is sketched in Figure 14c.

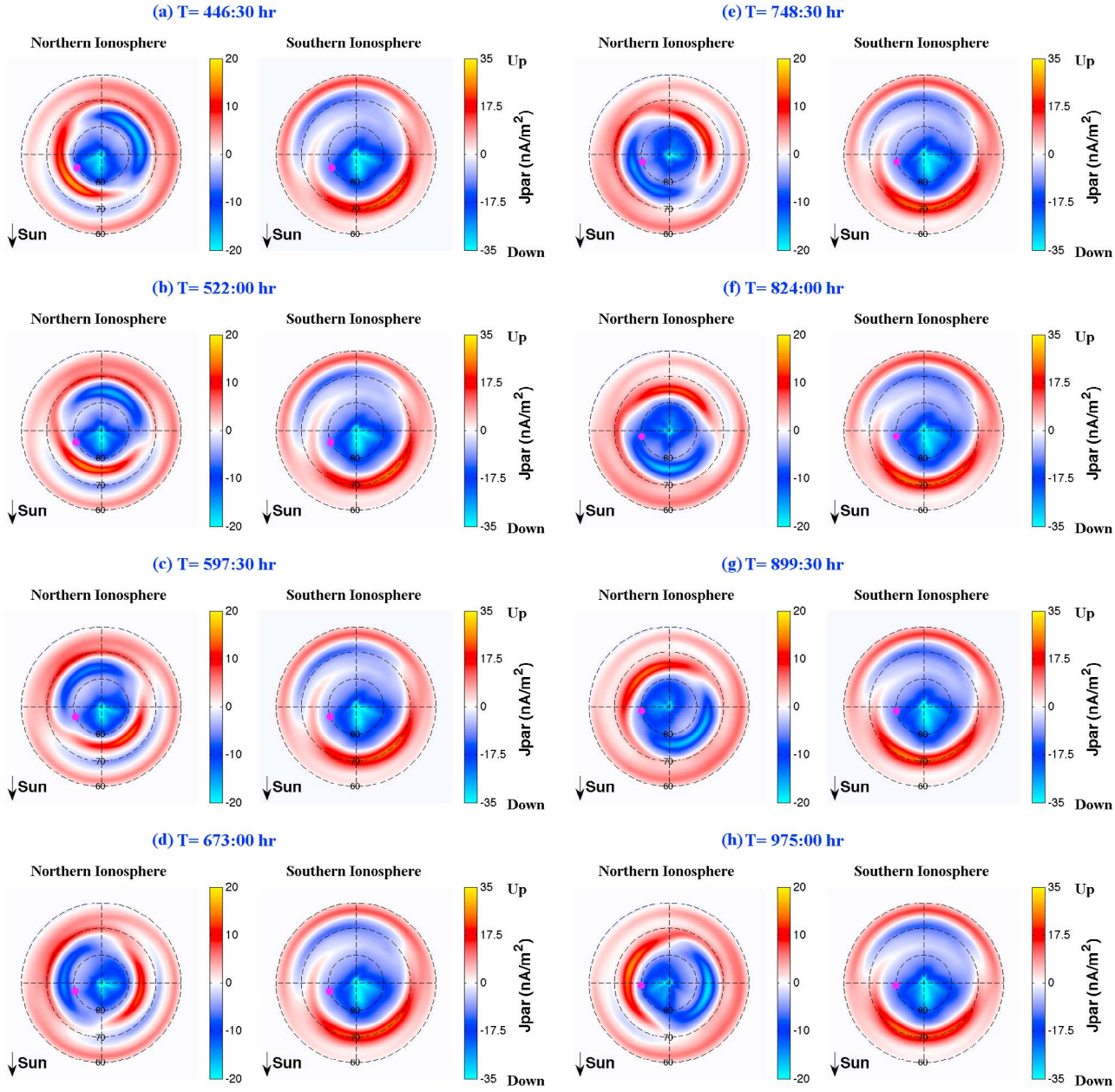

Figure 15. Ionospheric field-aligned currents (as in Figure 1) at the times of images in Figure 14.

times in the cycle. It is not clear whether these differences result from periodic variations of wave speeds or from a dependence on distance down the tail. The observations are, however, consistent with the statement that the density perturbations are initiated near -10 R_S when the upward field-aligned currents from the southern (northern) source are located near midnight. They grow in amplitude and propagate tailward, their centers reaching downtail distances between -15 and -20 R_S at about the time when the upward FACs from the ionosphere in the relevant hemisphere rotate into the dawn sector. At the location of the orbits in which periodic density enhancements have been reported by *Gurnett et al.* [2011], the center of the high-density region would typically occur within a few hours of SKR maximum, consistent with their phase analysis.

[33] Another approach can be used to demonstrate more directly that the periodicity of the bulges differs in the north and the south. In Figure 14, the images are separated by approximately 7 multiples of the southern period, i.e., 75.5 h or ~13% of a beat period. In Figures 14a–14h there is a bulge in the south at roughly the same x location, but from one frame to the next, the northern bulge shifts its x position. (Figure 15 showing the ionospheric current patterns at the times of Figures 14a–14h confirms that the southern phases differ little from one selected time step to another; they are all close to 100°, but the northern phases differ.) At the times shown in Figure 8, the phases of the northern and southern signals differ by less than 90° (see also Figure 9c) and plasma bulges in the north and south remain relatively close in phase in the vicinity of -15 R_S. This is not true at other

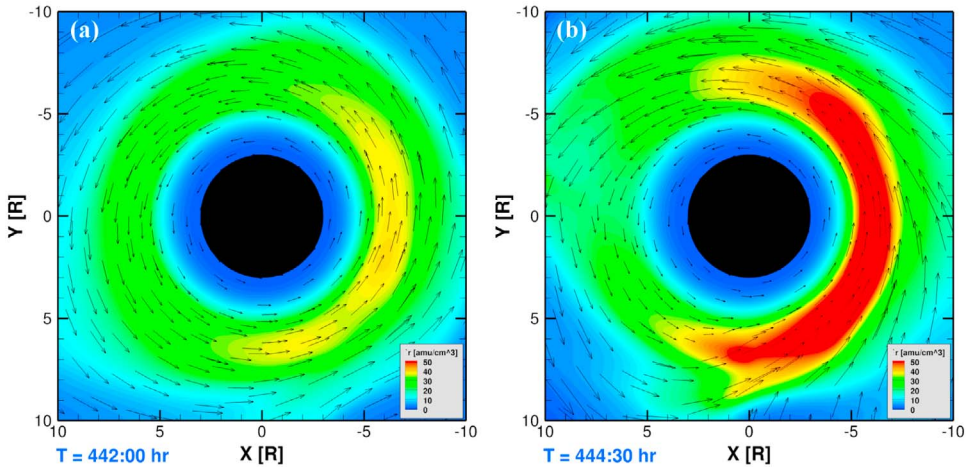

Figure 16. Plasma flow vectors (black arrows) and density (color) in Saturn's equatorial plane at times (a) 442:00 h and (b) 444:30 h in the MHD simulation of *Jia et al.* [2012b]. The solar wind dynamic pressure in the simulation increased rapidly (with changes in both density and velocity) from ~0.01 nPa to 0.17 nPa in 90 min. Figure 16b shows the response of the equatorial plasma 2.5 h after the start of the pressure increase.

times during the beat cycle. Although there is a density bulge on the southern boundary of the plasma sheet near $x = -15$ R_S in Figure 14, consistent with repetition of the generation of the bulge once every southern period, the location of the bulge in the northern hemisphere is located farther down tail than its southern partner in Figure 14a, but the separation in x of the northern and southern features diminishes in Figure 14b. The two bulges are almost aligned in Figure 14c at a time when the northern and southern signals are in antiphase as shown in Figure 15c. In Figures 14d–14g, the northern bulge lags the southern bulge in its journey down tail. This changing relative position in x is consistent with periodic generation of a bulge at slightly different periods in the two hemispheres.

6. The Issue of Phase Persistence

[34] In the model that we put forward in this paper, phase persistence is imposed by maintaining a constant rotation of the sources in the two hemispheres. That the phase of SKR does not experience persistent and random discontinuous jumps is supported by the observations plotted in Figure 1 of *Kurth et al.* [2008] that show a roughly constant mean phase of the southern SKR signal for almost 2 years from mid-2004 to mid-2006, an interval during which the southern period drifted slowly from slightly less to slightly more than 10.8 h [*Gurnett et al.*, 2010a; *Lamy*, 2011]. Further evidence of phase persistence is found in measurements of rotating magnetic perturbations in the equatorial middle magnetosphere. The equatorial magnetic field perturbations have been followed over many years [e.g., *Andrews et al.*, 2008, 2011, 2012; *Provan et al.*, 2011] and the phase at which the peak radial perturbations modulated at the southern SKR period point toward a specific local time has not jumped. We question whether such persistence of phase can be imposed by symmetry breaking through a purely magnetospheric process.

[35] If magnetospheric asymmetry is caused by an interchange instability, the persistence of phase requires the $m = 1$ pattern to form anew at a fixed rotation phase following global-scale disruptions of the magnetosphere of the sort known to occur in response to significant changes of solar wind properties. Is this the case? Unfortunately, spacecraft measurements cannot document the form of the global magnetospheric flow pattern at a given time, but we note that there is evidence that the solar wind can cause significant disruption of large parts of the magnetosphere. For example, simultaneous observations of the solar wind and Saturn's aurora show that both the size and intensity of the main auroral oval are subject to dramatic changes following the arrival of large solar wind disturbances, such as interplanetary shocks [*Clarke et al.*, 2005]. In addition, *Arridge et al.* [2011] in their investigation of flapping and other properties of the nightside plasma sheet discarded data from several passes (outbound rev 27 and rev 23) of a group of very similar passes. They remark that they do not analyze rev 27 outbound data because it "occurred during the passage of a CIR that produced considerable dynamics in the location of the plasma sheet." It is hard to imagine that the middle magnetosphere did not concurrently experience disruption in its rotational pattern.

[36] As global observations of convective flows are lacking, an approach to demonstrating the effect of the solar wind on magnetospheric convection patterns is to examine the response of the middle magnetosphere to an interplanetary shock in a global MHD simulation. For that purpose, we use the simulation described by *Jia et al.* [2012b]. They explore the response of the magnetosphere to changes of the dynamic pressure and the magnetic field properties of the solar wind, varying them through a range of parameters typical of the solar wind near the orbit of Saturn. We extract from the simulation the density and flow in the equatorial plane at two time steps. Prior to the first time (442:00 h), the IMF (0.5 nT) and plasma density (0.05 cm^{-3}) had been held constant for 90 h while the solar wind speed had been declining steadily from roughly 575 km/s to 400 km/s. At hour 442 a forward interplanetary shock arrives at the magnetosphere and the pressure jumps to 0.17 nPa while the IMF does not change. The second time step is taken 2.5 h later. Figure 16 shows

how the flow and the density distribution in the middle magnetosphere respond. Figure 16a shows the form of the plasma flow and the density in the equatorial plane at hour 442:00, just before the arrival of the shock. Figure 16b shows the same quantities at hour 444:30. It is evident in Figure 16 that following the arrival of the shock, the flow accelerates in much of the middle magnetosphere with strong local time variations and significant distortion of flow streamlines. We suggest that this distortion, initiated at a rotation phase determined only by the solar wind, will eliminate any memory of rotation phase in the magnetospheric plasma. It would seem that as the magnetosphere returns from this disturbed state to a quasi-steady state, an interchange instability could conceivably produce an $m = 1$ rotating flow structure (not present in the simulation), but it seems improbable that the rotation phase of such a pattern would return to its preshock value. It is for this reason that we argue that a convective flow pattern, which we agree is present in the equatorial magnetosphere, must be imposed from the elsewhere in the system in a region such as the upper atmosphere that is little disrupted by changes of the solar wind.

7. Discussion and Summary

[37] The model presented in this work is an extension of an earlier model of Saturn's rotational periodicity [*Jia et al.*, 2012a]. In our earlier work we explored the response of Saturn's magnetosphere to a rotating vortical structure centered in the high-latitude southern ionosphere and fixed in a frame rotating with a 10.8 h period. The period was selected to represent the southern SKR period of southern summer in 2005–2006 [*Lecacheux et al.*, 1997; *Kurth et al.*, 2007; *Gurnett et al.*, 2005, 2009a, 2009b, 2010a; *Lamy*, 2011]. We suggested that azimuthally asymmetric flows in the ionosphere are driven by collisions with structures embedded in the upper atmosphere. An MHD simulation of the model was successful in accounting for many observed periodic phenomena in the magnetosphere. The simulated magnetosphere responded with periodic inward-outward motion of the magnetopause, reproduced the up and back flapping of the magnetotail current sheet, and demonstrated an intensification of the FACs capable of driving SKR as the current upward from the ionosphere rotated into the morning sector. The model, however, did not include currents related to a northern hemisphere source of periodic SKR power. In this paper, we extend the earlier work by including an additional source of vortical flow in the northern hemisphere. The northern hemisphere structure is placed at slightly higher latitude than the southern structure and rotates about the spin axis with the 10.6 h period of the northern SKR signal in the years 2005–2006. The difference of the periods north and south might arise if the upper atmospheric sources were embedded in regions of slightly different zonal flow speeds, with the northern source embedded in winds rotating ~60 m/s faster than those in which the southern source was embedded. Differences of this magnitude in wind speeds are plausible as they are comparable with differences in zonal wind speeds measured in the troposphere [*Sánchez-Lavega et al.*, 2004]. One should ask whether a latitude asymmetry of 5° between the patterns in the north and the south of the upper atmosphere is plausible. Upper atmospheric properties are uncertain, but in the troposphere, wind patterns [*Sánchez-Lavega et al.*, 2004] are not symmetric across the equator, and at high latitudes, features north and south are shifted by of order 5°.

[38] In setting up the initial conditions for both the single and the dual source models, we imposed a very limited number of parameters to correspond to observations or expectations (conductance of southern and northern ionospheres selected to represent southern summer conditions, intensity of upward FACs selected to produce the magnitude of the observed magnetic perturbations inside of ~10 R_S, latitude selected to reflect localization of the cam current system) and we also assumed nominal solar wind conditions with a southward oriented IMF. Without any subsequent tweaking of model parameters, we obtain good quantitative agreement with observations.

[39] In the runs with dual sources, the magnetosphere's response is found to change through a 23 day period, the beat between the two imposed frequencies. Concentrating on the effects in the night side magnetosphere, we have identified various features of interest in the simulation. A beat period response is present in the amplitude of magnetic perturbations, with properties that vary with radial distance in the equatorial plane. The phase of the peaks of the oscillating perturbation magnetic field shifts over the beat period, corresponding well to the "jitter" reported by *Provan et al.* [2011]. The changing structure of the plasma sheet and the flapping of the current sheet correspond to observed thickening and north-south displacement reported by *Arridge et al.* [2011] and by *Provan et al.* [2012]. Propagating plasma bulges on the northern and southern boundaries of the plasma sheet account for the periodic plasma density enhancements at high invariant latitudes reported by *Gurnett et al.* [2010b, 2011] and provide an explanation of why the periods differ on the northern and southern boundaries of the plasma sheet.

[40] The success of the simulation in reproducing with good quantitative fidelity a large number of observed properties of Saturn's magnetosphere cannot be interpreted as proof that the ionosphere is the driver of the periodicity. The widely separated plasmas of the ionosphere and the equatorial magnetosphere are strongly coupled by FACs, and any process that imposes vortical flow on the magnetosphere will drive a corresponding ionospheric flow, the coupled system producing very similar responses to those we have extracted from the simulation in which the flows are imposed from the ionosphere into the magnetosphere. However, as we explain in section 6, we find it unlikely that the periodic processes that generate vortical flows in the equatorial magnetosphere would maintain phase coherence over long time intervals. We are also uncertain about how a signal at the rotation period is formed in the subcorotating plasma of the equatorial magnetosphere and we have not seen sufficient detail to understand how a pattern driven at the equator can be modulated to produce different periods in the north and south [*Southwood*, 2011a]. For these reasons, we continue to support the suggestion that the driver of the periodicities is a structure in the upper atmosphere, not yet observed or described theoretically, that couples collisionally into the ionosphere and is largely unaffected by changes in the solar wind.

[41] Specifics of the flows capable of driving magnetospheric oscillations of the magnitude required by observation are sensitive to the conductivity of the ionosphere, a

quantity that is not well constrained. In the present study, we used values of Pedersen conductances (1 S for the northern hemisphere and 3 S for the southern hemisphere) that are close to recent estimates from calculations using Cassini RSS measurements [*Moore et al.*, 2010] and theoretical studies [*Bunce et al.*, 2003; *Cowley et al.*, 2008] using magnetospheric flow measurements together with inferences from images of the aurora. However, *Galand et al.* [2011] propose somewhat higher ionospheric conductance than that used in this paper. *Ray et al.* [2012] propose a large range of conductances from 3.0 to 18.9 S at the latitudes of importance for our analysis. With higher conductance and proportionately lower wind speeds, identical FACs would be generated by the vortical flow pattern. In future work, we intend to test whether such ionospheric conditions would affect the large-scale properties of the magnetosphere significantly.

[42] During approach to equinox in 2009 the frequencies of the northern and southern SKR signals converged [*Gurnett et al.*, 2009a, 2009b, 2010a; *Lamy*, 2011; *Andrews et al.*, 2012]. After equinox the conductivity in the northern hemisphere should have increased while the conductivity in the south should have decreased. If our model is valid, one would expect that such changes would affect the relative amplitudes of the fluctuations driven by the northern and southern sources. (*Andrews et al.* [2012] report that the ratio of the amplitudes of the northern and southern magnetic perturbations in the core region became as large as 0.87 in 2008 and became comparable postequinox.) How the seasonal changes in illumination will affect the upper atmosphere is uncertain, but that seasonal changes will affect magnetospheric dynamics is highly probable. In future studies we intend to investigate seasonal changes and also to allow a varying solar wind to modify the magnetosphere's response to the internal processes that impose rotational periodicity.

Appendix A: The Global MHD Model

[43] This appendix describes key features of the global MHD model used in this study. BATSRUS [*Powell et al.*, 1999; *Gombosi et al.*, 2002, 2004] solves the governing MHD equations (conservation of mass, momentum and energy together with Faraday's law) with a near-conservative finite volume method. BATSRUS has been adapted to model Saturn's magnetosphere by including mass-loading source terms in the MHD equations (for details, see *Hansen et al.* [2000]) and further improved by adjusting the spatial distribution of internal plasma sources as well as the mass-loading rates according to recent observations [*Hansen et al.*, 2005]. Specifically, the main plasma source of water group ions W^+ (H_2O^+, OH^+, O^+, H_3O^+) originating from Enceladus and the rings is included in the global model as an axisymmetric disc-like source centered at $\sim$5.35 R_S (R_S, radius of Saturn = 60,268 km) [*Richardson et al.*, 1998], while a secondary plasma source of nitrogen ions N^+ originating from Titan is included as an axisymmetric torus around Titan's orbit at $\sim$20 R_S. A nominal total ionization rate of $\sim 6 \times 10^{27}$ s^{-1} for W^+ and $\sim 5 \times 10^{25}$ s^{-1} for N^+ is used in the present study, corresponding to a total ionization rate of plasma of $\sim$170 kg/s assuming an average mass of 16.6 amu for W^+ and 14 amu for N^+. In addition to the ionization source term, we also include the source term associated with charge exchange, a process that does not contribute to plasma density but modifies the momentum of the plasma. The charge exchange rate in our model is computed based on the results of *Richardson et al.* [1998] that provide information about the oxygen neutral density (peaks at $\sim$4 R_S) and the reaction rate. The total charge exchange rate used is $\sim$70 kg/s.

[44] In our model, the coupling of the global magnetosphere (modeled by BATSRUS) and the ionosphere (modeled by IE [*Ridley et al.*, 2004]) is handled through FACs in a relatively simplified way that is used in most Earth magnetosphere models [*Raeder et al.*, 1998; *Ridley et al.*, 2004; *Tóth et al.*, 2005; *Lyon et al.*, 2004; *Hu et al.*, 2007]. Field-aligned currents are calculated in the magnetosphere at 4 R_S, about 1 R_S beyond the inner boundary of the magnetospheric domain, and then mapped into the ionosphere at $\sim$1 R_S along dipole field lines. Owing to the continuity of electric current, field-aligned currents must close through horizontal currents in the ionosphere, which is approximated by a height-integrated resistive layer located at $\sim$1000 km above the 1 mbar level. Closure currents in the ionosphere are then used to derive the distribution of the electric potential and hence the electric field for a given distribution of ionospheric conductance (including both Pedersen and Hall conductances) using a Poisson's solver in the IE model. The ionospheric electric field thus obtained is mapped back along dipole field lines from the ionosphere to the inner boundary of the magnetosphere under the ideal MHD assumption that magnetic field lines are equipotentials. The resulting electric field is then used to modify the $\mathbf{E} \times \mathbf{B}/|B|^2$ drift velocity at the inner boundary, thus allowing the interaction with the ionosphere to act back on the magnetosphere. The rigid corotation flow pattern for a given rotation rate of the planet (Saturn's rotation period is set as 648 min, or 10.8 h, consistent with the southern SKR period for late 2005 and early 2006 [*Gurnett et al.*, 2009b]) is then superimposed onto the calculated convection modulation to obtain a modified convection pattern. The modified flow, which is the sum of rigid corotation and the modification due to the interaction between the magnetosphere and ionosphere, sets the transverse velocity components at the inner boundary of the global MHD model. At the inner simulation boundary (at 3 R_S), we set the mass density to 0.1 amu/cm^3 and the temperature to 3 eV.

[45] In addition to the FACs derived from the global magnetosphere model, the ionospheric conductance is a required input parameter in the IE model. Initial estimates of the ionospheric Pedersen conductance, mainly based on Voyager era radio occultations and modeled ionospheric electron density profiles, gave a wide range from 0.1 S to 100 S [*Connerney et al.*, 1983; *Atreya et al.*, 1984; *Cheng and Waite*, 1988]. Recent estimates from calculations using Cassini RSS measurements [*Moore et al.*, 2010] and theoretical studies [*Bunce et al.*, 2003; *Cowley et al.*, 2008] using magnetospheric flow measurements together with auroral observations suggest an ionospheric Pedersen conductance of several siemens. *Ray et al.* [2012] favor higher ionospheric conductances, between 3.0 and 18.9 S. At this stage, it is evident that the conductances are uncertain. However, for higher conductances, the speed imposed in ionospheric flow perturbations would have to be reduced so that the

perturbation magnetic field near the equator would correspond to observations. Thus, it is not apparent how sensitive our results are to the specific conductances selected, although they are surely sensitive to the ratio between values imposed in the north and the south. Here we have set the Pedersen conductance to 1 S in the northern ionosphere and 3 S in the southern hemisphere to represent the southern summer season. The Hall conductances in the two ionospheres are set to zero for simplicity. In future work, we desire to test the sensitivity of the magnetospheric response to the ionospheric conductance.

[46] BATSRUS has the capability to use generalized curvilinear coordinates, which provide a smooth mapping from a logically Cartesian grid to an arbitrary curvilinear grid, including spherical, cylindrical and toroidal grids [*Tóth et al.*, 2012]. Our present model adopts a high-resolution nonuniform spherical grid, which provides fine resolution in regions of interest such as the inner magnetosphere and the magnetospheric boundaries (e.g., the bow shock and the magnetopause). The grid resolution around the main mass-loading region associated with Enceladus' neutral cloud ranges from $\sim$0.2 R_S between 5 and 10 R_S to 0.5 R_S near Titan's orbit (at $\sim$20 R_S). A high-resolution grid with 0.5° resolution in colatitude (θ) and 1° resolution in longitude (ϕ) is adopted for the IE solver. The global simulation is advanced in time with a fixed time step of 30 s and is run for an extended interval of $\sim$1000 h in order to investigate the interaction between the two atmospheric sources over a beat cycle.

[47] **Acknowledgments.** We thank Tamas Gombosi for useful discussions and for establishing a powerful computational framework without which this work could not have been undertaken. This work was supported by NASA through grants NNX12AK34G at the University of Michigan (X.J. and M.G.K.) and NNX10AF16G at UCLA (M.G.K.) and by the Cassini mission under contracts JPL 1409449 (X.J.) and 1416974 (M.G.K.) The simulation presented in this study was performed on the Pleiades supercomputer managed by the NASA Advanced Supercomputing division.

[48] Masaki Fujimoto thanks the reviewers for their assistance in evaluating this paper.

References

Anderson, J. D., and G. Schubert (2007), Saturn's gravitational field, internal rotation, and interior structure, *Science*, *317*, 1384–1387, doi:10.1126/science.1144835.

Andrews, D. J., E. J. Bunce, S. W. H. Cowley, M. K. Dougherty, G. Provan, and D. J. Southwood (2008), Planetary period oscillations in Saturn's magnetosphere: Phase relation of equatorial magnetic field oscillations and SKR modulation, *J. Geophys. Res.*, *113*, A09205, doi:10.1029/2007JA012937.

Andrews, D. J., S. W. H. Cowley, M. K. Dougherty, and G. Provan (2010a), Magnetic field oscillations near the planetary period in Saturn's equatorial magnetosphere: Variation of amplitude and phase with radial distance and local time, *J. Geophys. Res.*, *115*, A04212, doi:10.1029/2009JA014729.

Andrews, D. J., A. J. Coates, S. W. H. Cowley, M. K. Dougherty, L. Lamy, G. Provan, and P. Zarka (2010b), Magnetospheric period oscillations at Saturn: Comparison of equatorial and high latitude magnetic field periods with north and south SKR periods, *J. Geophys. Res.*, *115*, A12252, doi:10.1029/2010JA015666.

Andrews, D. J., B. Cecconi, S. W. H. Cowley, M. K. Dougherty, L. Lamy, G. Provan, and P. Zarka (2011), Planetary period oscillations at Saturn: Evidence in magnetic field phase data for rotational modulation of Saturn kilometric radiation emissions, *J. Geophys. Res.*, *116*, A09206, doi:10.1029/2011JA016636.

Andrews, D. J., S. W. H. Cowley, M. K. Dougherty, L. Lamy, G. Provan, and D. J. Southwood (2012), Planetary period oscillations in Saturn's magnetosphere: Evolution of magnetic oscillation properties from southern summer to post-equinox, *J. Geophys. Res.*, *117*, A04224, doi:10.1029/2011JA017444.

Arridge, C. S., K. K. Khurana, C. T. Russell, D. J. Southwood, N. Achilleos, M. K. Dougherty, A. J. Coates, and H. K. Leinweber (2008), Warping of Saturn's magnetospheric and magnetotail current sheets, *J. Geophys. Res.*, *113*, A08217, doi:10.1029/2007JA012963.

Arridge, C. S., et al. (2011), Periodic motion of Saturn's nightside plasma sheet, *J. Geophys. Res.*, *116*, A11205, doi:10.1029/2011JA016827.

Atreya, S. K., T. M. Donahue, A. F. Nagy, J. H. Waite Jr., and J. C. McConnell (1984), Theory, measurements, and models of the upper atmosphere and ionosphere of Saturn, in *Saturn*, edited by T. Gehrels and M. S. Matthews, pp. 239–277, Univ. of Ariz. Press, Tucson.

Bunce, E. J., S. W. H. Cowley, and J. A. Wild (2003), Azimuthal magnetic fields in Saturn's magnetosphere: Effects associated with plasma subcorotation and the magnetopause-tail current system, *Ann. Geophys.*, *21*, 1709–1722, doi:10.5194/angeo-21-1709-2003.

Carbary, J. F., and S. M. Krimigis (1982), Charged particle periodicity in the Saturnian magnetosphere, *Geophys. Res. Lett.*, *9*, 1073–1076, doi:10.1029/GL009i009p01073.

Carbary, J. F., D. G. Mitchell, S. M. Krimigis, and N. Krupp (2007), Evidence for spiral pattern in Saturn's magnetosphere using the new SKR longitudes, *Geophys. Res. Lett.*, *34*, L13105, doi:10.1029/2007GL030167.

Carbary, J. F., D. G. Mitchell, P. Brandt, E. C. Roelof, and S. M. Krimigis (2008), Periodic tilting of Saturn's plasma sheet, *Geophys. Res. Lett.*, *35*, L24101, doi:10.1029/2008GL036339.

Cecconi, B., L. Lamy, P. Zarka, R. Prange', W. S. Kurth, and P. Louarn (2009), Goniopolarimetric study of the revolution 29 perikrone using the Cassini Radio and Plasma Wave Science instrument high-frequency radio receiver, *J. Geophys. Res.*, *114*, A03215, doi:10.1029/2008JA013830.

Cheng, A. F., and J. H. Waite (1988), Corotation lag of Saturn's magnetosphere: Global ionospheric conductivities revisited, *J. Geophys. Res.*, *93*, 4107–4109, doi:10.1029/JA093iA05p04107.

Clarke, J. T., et al. (2005), Morphological differences between Saturn's ultraviolet aurorae and those of Earth and Jupiter, *Nature*, *433*, 717–719, doi:10.1038/nature03331.

Clarke, K. E., D. J. Andrews, A. J. Coates, S. W. H. Cowley, and A. Masters (2010a), Magnetospheric period oscillations of Saturn's bow shock, *J. Geophys. Res.*, *115*, A05202, doi:10.1029/2009JA015164.

Clarke, K. E., D. J. Andrews, C. S. Arridge, A. J. Coates, and S. W. H. Cowley (2010b), Magnetopause oscillations near the planetary period at Saturn: Occurrence, phase, and amplitude, *J. Geophys. Res.*, *115*, A08209, doi:10.1029/2009JA014745.

Connerney, J. E. P., M. H. Acuna, and N. F. Ness (1983), Currents in Saturn's magnetosphere, *J. Geophys. Res.*, *88*, 8779–8789, doi:10.1029/JA088iA11p08779.

Cowley, S. W. H., D. M. Wright, E. J. Bunce, A. C. Carter, M. K. Dougherty, G. Giampieri, J. D. Nichols, and T. R. Robinson (2006), Cassini observations of planetary-period magnetic field oscillations in Saturn's magnetosphere: Doppler shifts and phase motion, *Geophys. Res. Lett.*, *33*, L07104, doi:10.1029/2005GL025522.

Cowley, S. W. H., C. S. Arridge, E. J. Bunce, J. T. Clarke, A. J. Coates, M. K. Dougherty, J. Gérard, D. Grodent, J. D. Nichols, and D. L. Talboys (2008), Auroral current systems in Saturn's magnetosphere: Comparison of theoretical models with Cassini and HST observations, *Ann. Geophys.*, *26*, 2613–2630, doi:10.5194/angeo-26-2613-2008.

Desch, M. D., and M. L. Kaiser (1981), Voyager measurement of the rotation period of Saturn's magnetic field, *Geophys. Res. Lett.*, *8*, 253–256, doi:10.1029/GL008i003p00253.

Dougherty, M. K., et al. (2004), The Cassini magnetic field investigation, *Space Sci. Rev.*, *114*, 331–383, doi:10.1007/s11214-004-1432-2.

Espinosa, S. A., and M. K. Dougherty (2000), Periodic perturbations in Saturn's magnetic field, *Geophys. Res. Lett.*, *27*, 2785–2788, doi:10.1029/2000GL000048.

Espinosa, S. A., D. J. Southwood, and M. K. Dougherty (2003a), Reanalysis of Saturn's magnetospheric field data view of spin-periodic perturbations, *J. Geophys. Res.*, *108*(A2), 1085, doi:10.1029/2001JA005083.

Espinosa, S. A., D. J. Southwood, and M. K. Dougherty (2003b), How can Saturn impose its rotation period in a noncorotating magnetosphere?, *J. Geophys. Res.*, *108*(A2), 1086, doi:10.1029/2001JA005084.

Galand, M., L. Moore, I. Müller-Wodarg, M. Mendillo, and S. Miller (2011), Response of Saturn's auroral ionosphere to electron precipitation: Electron density, electron temperature, and electrical conductivity, *J. Geophys. Res.*, *116*, A09306, doi:10.1029/2010JA016412.

Galopeau, P. H. M., and A. Lecacheux (2000), Variations of Saturn's radio rotation period measured at kilometer wavelengths, *J. Geophys. Res.*, *105*, 13,089–13,102, doi:10.1029/1999JA005089.

Goldreich, P., and A. J. Farmer (2007), Spontaneous axisymmetry breaking of the external magnetic field at Saturn, *J. Geophys. Res.*, *112*, A05225, doi:10.1029/2006JA012163.

Gombosi, T. I., and K. C. Hansen (2005), Saturn's variable magnetosphere, *Science*, *307*, 1224–1226, doi:10.1126/science.1108226.

Gombosi, T. I., G. Tóth, D. L. de Zeeuw, K. C. Hansen, K. Kabin, and K. G. Powell (2002), Semi-relativistic magnetohydrodynamics and physics-based convergence acceleration, *J. Comput. Phys.*, *177*, 176–205, doi:10.1006/jcph.2002.7009.

Gombosi, T. I., et al. (2004), Solution-adaptive magnetohydrodynamics for space plasmas: Sun to Earth simulations, *Comput. Sci. Eng.*, *6*(2), 14–35, doi:10.1109/MCISE.2004.1267603.

Gurnett, D. A., et al. (2004), The Cassini radio and plasma wave science investigation, *Space Sci. Rev.*, *114*, 395–463, doi:10.1007/s11214-004-1434-0.

Gurnett, D. A., et al. (2005), Radio and plasma wave observations at Saturn from Cassini's approach and first orbit, *Science*, *307*, 1255–1259, doi:10.1126/science.1105356.

Gurnett, D. A., A. M. Persoon, W. S. Kurth, J. B. Groene, T. F. Averkamp, M. K. Dougherty, and D. J. Southwood (2007), The variable rotation period of the inner region of Saturn's plasma disk, *Science*, *316*, 442–445, doi:10.1126/science.1138562.

Gurnett, D. A., A. M. Persoon, J. B. Groene, A. J. Kopf, G. B. Hospodarsky, and W. S. Kurth (2009a), A north-south difference in the rotation rate of auroral hiss at Saturn: Comparison to Saturn's kilometric radio emission, *Geophys. Res. Lett.*, *36*, L21108, doi:10.1029/2009GL040774.

Gurnett, D. A., A. Lecacheux, W. S. Kurth, A. M. Persoon, J. B. Groene, L. Lamy, P. Zarka, and J. F. Carbary (2009b), Discovery of a north-south asymmetry in Saturn's radio rotation period, *Geophys. Res. Lett.*, *36*, L16102, doi:10.1029/2009GL039621.

Gurnett, D. A., J. B. Groene, A. M. Persoon, J. D. Menietti, S.-Y. Ye, W. S. Kurth, R. J. MacDowall, and A. Lecacheux (2010a), The reversal of the rotational modulation rates of the north and south components of Saturn kilometric radiation near equinox, *Geophys. Res. Lett.*, *37*, L24101, doi:10.1029/2010GL045796.

Gurnett, D. A., et al. (2010b), A plasmapause-like density boundary at high latitudes in Saturn's magnetosphere, *Geophys. Res. Lett.*, *37*, L16806, doi:10.1029/2010GL044466.

Gurnett, D. A., A. M. Persoon, J. B. Groene, W. S. Kurth, M. Morooka, J.-E. Wahlund, and J. D. Nichols (2011), The rotation of the plasmapause-like boundary at high latitudes in Saturn's magnetosphere and its relation to the eccentric rotation of the northern and southern auroral ovals, *Geophys. Res. Lett.*, *38*, L21203, doi:10.1029/2011GL049547.

Hansen, K. C., T. I. Gombosi, D. Dezeeuw, C. P. T. Groth, and K. G. Powell (2000), A 3D global MHD simulation of Saturn's magnetosphere, *Adv. Space Res.*, *26*, 1681–1690, doi:10.1016/S0273-1177(00)00078-8.

Hansen, K. C., A. J. Ridley, G. B. Hospodarsky, N. Achilleos, M. K. Dougherty, T. I. Gombosi, and G. Tóth (2005), Global MHD simulations of Saturn's magnetosphere at the time of Cassini approach, *Geophys. Res. Lett.*, *32*, L20S06, doi:10.1029/2005GL022835.

Hill, T. W. (1979), Inertial limit on corotation, *J. Geophys. Res.*, *84*, 6554–6558, doi:10.1029/JA084iA11p06554.

Hu, Y. Q., X. C. Guo, and C. Wang (2007), On the ionospheric and reconnection potentials of the Earth: Results from global MHD simulations, *J. Geophys. Res.*, *112*, A07215, doi:10.1029/2006JA012145.

Jia, X., M. G. Kivelson, and T. I. Gombosi (2012a), Driving Saturn's magnetospheric periodicities from the upper atmosphere/ionosphere, *J. Geophys. Res.*, *117*, A04215, doi:10.1029/2011JA017367.

Jia, X., K. C. Hansen, T. I. Gombosi, M. G. Kivelson, G. Tóth, D. L. DeZeeuw, and A. J. Ridley (2012b), Magnetospheric configuration and dynamics of Saturn's magnetosphere: A global MHD simulation, *J. Geophys. Res.*, *117*, A05225, doi:10.1029/2012JA017575.

Khurana, K. K., D. G. Mitchell, C. S. Arridge, M. K. Dougherty, C. T. Russell, C. Paranicas, N. Krupp, and A. J. Coates (2009), Sources of rotational signals in Saturn's magnetosphere, *J. Geophys. Res.*, *114*, A02211, doi:10.1029/2008JA013312.

Kurth, W. S., A. Lecacheux, T. F. Averkamp, J. B. Groene, and D. A. Gurnett (2007), A Saturnian longitude system based on a variable kilometric radiation period, *Geophys. Res. Lett.*, *34*, L02201, doi:10.1029/2006GL028336.

Kurth, W. S., T. F. Averkamp, D. A. Gurnett, J. B. Groene, and A. Lecacheux (2008), An update to a Saturnian longitude system based on kilometric radio emissions, *J. Geophys. Res.*, *113*, A05222, doi:10.1029/2007JA012861.

Lamy, L. (2011), Variability of southern and northern SKR periodicities, in *Planetary Radio Emissions VII*, edited by H. O. Rucker et al., pp. 39–50, Austrian Acad. of Sci. Press, Vienna, doi:10.1553/PRE7s39.

Lamy, L., B. Cecconi, R. Prange, P. Zarka, J. D. Nichols, and J. T. Clarke (2009), An auroral oval at the footprint of Saturn's kilometric radio sources, colocated with the UV aurorae, *J. Geophys. Res.*, *114*, A10212, doi:10.1029/2009JA014401.

Lecacheux, A., P. Galopeau, and M. Aubier (1997), Re-visiting Saturnian radiation with Ulysses/URAP, in *Planetary Radio Emissions IV*, edited by H. O. Rucker, S. J. Bauer, and A. Lecacheux, pp. 313–325, Austrian Acad. of Sci. Press, Vienna.

Lyon, J. G., J. A. Fedder, and C. M. Mobarry (2004), The Lyon-Fedder-Mobarry (LFM) global MHD magnetospheric simulation code, *J. Atmos. Sol. Terr. Phys.*, *66*, 1333–1350, doi:10.1016/j.jastp.2004.03.020.

Mitchell, D. G., et al. (2009), Recurrent energization of plasma in the midnight-to-dawn quadrant of Saturn's magnetosphere, and its relationship to auroral UV and radio emissions, *Planet. Space Sci.*, *57*, 1732–1742, doi:10.1016/j.pss.2009.04.002.

Moore, L., I. Mueller-Wodarg, M. Galand, A. Kliore, and M. Mendillo (2010), Latitudinal variations in Saturn's ionosphere: Cassini measurements and model comparisons, *J. Geophys. Res.*, *115*, A11317, doi:10.1029/2010JA015692.

Morooka, M. W., et al. (2009), The electron density of Saturn's magnetosphere, *Ann. Geophys.*, *27*, 2971–2991, doi:10.5194/angeo-27-2971-2009.

Nichols, J. D., S. W. H. Cowley, and L. Lamy (2010), Dawn-dusk oscillation of Saturn's conjugate auroral ovals, *Geophys. Res. Lett.*, *37*, L24102, doi:10.1029/2010GL045818.

Powell, K. G., P. L. Roe, T. J. Linde, T. I. Gombosi, and D. L. DeZeeuw (1999), A solution-adaptive upwind scheme for ideal magnetohydrodynamics, *J. Comput. Phys.*, *154*, 284–309, doi:10.1006/jcph.1999.6299.

Provan, G., S. W. H. Cowley, and J. D. Nichols (2009), Phase relation of oscillations near the planetary period of Saturn's auroral oval and the equatorial magnetospheric magnetic field, *J. Geophys. Res.*, *114*, A04205, doi:10.1029/2008JA013988.

Provan, G., D. J. Andrews, B. Cecconi, S. W. H. Cowley, M. K. Dougherty, L. Lamy, and P. M. Zarka (2011), Magnetospheric period magnetic field oscillations at Saturn: Equatorial phase "jitter" produced by superposition of southern and northern period oscillations, *J. Geophys. Res.*, *116*, A04225, doi:10.1029/2010JA016213.

Provan, G., D. J. Andrews, C. S. Arridge, A. J. Coates, S. W. H. Cowley, G. Cox, M. K. Dougherty, and C. M. Jackman (2012), Dual periodicities in planetary-period magnetic field oscillations in Saturn's tail, *J. Geophys. Res.*, *117*, A01209, doi:10.1029/2011JA017104.

Raeder, J., J. Berchem, and M. Ashour-Abdalla (1998), The geospace environment modeling grand challenge: Results from a global geospace circulation model, *J. Geophys. Res.*, *103*, 14,787–14,797, doi:10.1029/98JA00014.

Ray, L. C., M. Galand, L. Moore, and B. L. Fleshman (2012), Characterizing the limitations to the coupling between Saturn's ionosphere and middle magnetosphere, *J. Geophys. Res.*, *117*, A07210, doi:10.1029/2012JA017735.

Richardson, J. D., A. Eviatar, M. A. McGrath, and V. M. Vasyliunas (1998), OH in Saturn's magnetosphere: Observations and implications, *J. Geophys. Res.*, *103*, 20,245–20,255, doi:10.1029/98JE01127.

Ridley, A., T. I. Gombosi, and D. DeZeeuw (2004), Ionospheric control of the magnetosphere: Conductance, *Ann. Geophys.*, *22*, 567–584, doi:10.5194/angeo-22-567-2004.

Sánchez-Lavega, A., R. Huesoa, S. Pérez-Hoyos, J. F. Rojas, and R. G. French (2004), Saturn's cloud morphology and zonal winds before the Cassini encounter, *Icarus*, *170*, 519–523, doi:10.1016/j.icarus.2004.05.002.

Seidelmann, P. K., et al. (2002), Report of the IAU/IAG working group on cartographic coordinates and rotational elements of the planets and satellites: 2000, *Celestial Mech. Dyn. Astron.*, *82*, 83–111, doi:10.1023/A:1013939327465.

Southwood, D. (2011a), Direct evidence of differences in magnetic rotation rate between Saturn's northern and southern polar regions, *J. Geophys. Res.*, *116*, A01201, doi:10.1029/2010JA016070.

Southwood, D. J. (2011b), Ionospheric-magnetospheric coupling and the creation of dual periodicity in Saturnian magnetospheric dynamics, Abstract SM13F-03 presented at 2011 Fall Meeting, AGU, San Francisco, Calif., 5–9 Dec.

Southwood, D. J., and M. G. Kivelson (2007), Saturnian magnetospheric dynamics: Elucidation of a camshaft model, *J. Geophys. Res.*, *112*, A12222, doi:10.1029/2007JA012254.

Southwood, D. J., and M. G. Kivelson (2009), The source of Saturn's periodic radio emission, *J. Geophys. Res.*, *114*, A09201, doi:10.1029/2008JA013800.

Thomsen, M. F., D. B. Reisenfeld, D. M. Delapp, R. L. Tokar, D. T. Young, F. J. Crary, E. C. Sittler, M. A. McGraw, and J. D. Williams (2010), Survey of ion plasma parameters in Saturn's magnetosphere, *J. Geophys. Res.*, *115*, A10220, doi:10.1029/2010JA015267.

Tóth, G., et al. (2005), Space Weather Modeling Framework: A new tool for the space science community, *J. Geophys. Res.*, *110*, A12226, doi:10.1029/2005JA011126.

Tóth, G., et al. (2012), Adaptive numerical algorithms in space weather modeling, *J. Comput. Phys.*, *231*, 870–903, doi:10.1016/j.jcp.2011.02.006.

Vasyliūnas, V. M. (1983), Plasma distribution and flow, in *Physics of the Jovian Magnetosphere*, edited by A. J. Dessler, pp. 395–453, Cambridge Univ. Press, New York, doi:10.1017/CBO9780511564574.013.

Warwick, J. W., et al. (1981), Planetary radio astronomy observations from Voyager 1 near Saturn, *Science*, *212*, 239–243, doi:10.1126/science.212.4491.239.

Zieger, B., K. C. Hansen, T. I. Gombosi, and D. L. DeZeeuw (2010), Periodic plasma escape from the mass-loaded Kronian magnetosphere, *J. Geophys. Res.*, *115*, A08208, doi:10.1029/2009JA014951.